

A Hierarchical Control Strategy With Fault Ride-Through Capability for Variable Frequency Transformer

Bharath Babu Ambati, Parag Kanjiya, Vinod Khadkikar, *Member, IEEE*,
Mohamed Shawky El-Moursi, *Member, IEEE*, and James L. Kirtley Jr., *Fellow, IEEE*

Abstract—A variable frequency transformer (VFT) is being considered as a new alternative to the classical back-to-back high voltage direct current (HVDC) system for interconnection of two asynchronous networks. The VFT is a retrospective form of frequency converter using the wound rotor induction machine (WRIM), which converts the constant frequency input into a variable frequency output. The prime objective of VFT is to achieve controlled bidirectional power transfer between the two asynchronous networks. This paper presents a detailed working principle of VFT technology and proposes a new hierarchical control strategy for establishing the VFT connection with two power systems to achieve bidirectional power transfer between them. Also, to restrict the grid fault propagation from one side of the VFT to the other side, a series dynamic braking resistor based fault ride-through (FRT) scheme is proposed. The performance of the VFT during synchronization process, steady-state, dynamic, and the grid fault conditions is evaluated using the real-time hardware in-loop (HIL) system. The plant is simulated in real time using OPAL-RT real-time simulator while the control algorithm is implemented in digital signal processor to carry out HIL study. All the important results supporting the effectiveness of the proposed control strategy and FRT scheme are discussed.

Index Terms—Fault propagation, hierarchical control, power flow control, rotating transformer, series dynamic breaking resistor (SDBR), variable frequency transformer (VFT).

I. INTRODUCTION

IN GENERAL, the interconnection of two different power networks with controlled power transfer capability can be achieved by a synchronous tie using a phase-shifting transformer or by an asynchronous tie using classical back-to-back high voltage direct current (HVDC) link. In the modern power systems, establishing a synchronous tie between two power networks would be a challenging task especially when one or both the networks experience a slight variation in their frequencies [1]. Moreover, the use of phase-shifting transformers in synchronous ties suffers from the drawbacks such as slow and

step-wise controls [2]. This further causes wear and tear of tap changer contacts. Although, the use of power electronic controlled phase-shifting transformer can eliminate these drawbacks, they introduce additional problems such as harmonics, resonance, vulnerability to voltage surges, and reduced overloading capability due to their low thermal time constant [2], [3]. On the other hand, a back-to-back HVDC link can be established between any two power networks to achieve the controlled power flow between them. A line commutated converter (LCC)-based HVDC link suffers with the bottlenecks such as large reactive power requirements, lower thermal time constant, and lack of inertia for natural damping. Whereas, the voltage source converter (VSC)-based HVDC link can control the reactive power unlike LCC-based HVDC link. But, the inertia contribution and frequency response are still the challenges for HVDC technologies. Alternatively, the use of variable frequency transformer (VFT) for asynchronous interconnection can improve the system inertia and frequency control.

The VFT was first developed by General Electric Company in 2004 to achieve the interconnection of two different power networks [2]. A VFT is a controllable bidirectional power transfer device between the two asynchronous power networks that consists of wound rotor induction machine (WRIM) and a dc motor drive [2]. The presence of rotating mass (of both WRIM and dc motor) adds inertia to the power systems and thereby improves the stability during system disturbances. The VFT offers significant benefits over the widely installed LCC-HVDC link [4]–[6], mainly, lower reactive power requirements, harmonic-free power transfer, and higher system stability.

Basic concept and design aspects of 100 MW VFT is presented in [2]. The performance of VFT during steady-state, dynamic, and transient conditions is evaluated using simulation studies in [7]–[12]. In [13], the offshore wind park is connected to the grid through VFT to reduce the power fluctuations using the PID damping torque controller of the dc motor drive. Moreover, the use of brushless doubly fed induction machine (BDFIM) with squirrel cage rotor as alternative VFT configuration is reported in [6]. In which, the dual stator winding with different pole numbers with a ratio of 1:3 is used to avoid space harmonics concerns. The operating performance and maintenance of VFT is discussed in [15] and [16].

The steady-state analysis of the VFT is well established in the literature [2]–[12], but the problem of fault propagation and the fault ride-through (FRT) enhancement is not addressed so far. As

Manuscript received October 28, 2013; revised February 27, 2014 and May 19, 2014; accepted June 21, 2014. Paper no. TEC-00638-2013.

B. B. Ambati, P. Kanjiya, and V. Khadkikar are with the Center for Energy, Masdar Institute of Science and Technology, Abu Dhabi, 54224, UAE (e-mail: bambati@masdar.ac.ae; pkanjiya@masdar.ac.ae; vkhadkikar@masdar.ac.ae).

M. S. El-Moursi and J. L. Kirtley Jr. are with the Department of Electrical Engineering and Computer Science, Massachusetts Institute of Technology, Cambridge, MA 02139 USA. (e-mail: melmoursi@mit.edu; kirtley@mit.edu).

Color versions of one or more of the figures in this paper are available online at <http://ieeexplore.ieee.org>.

Digital Object Identifier 10.1109/TEC.2014.2336981

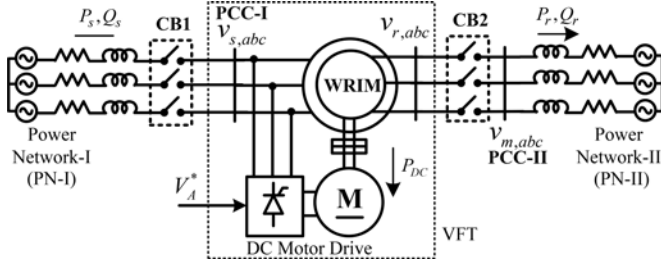


Fig. 1. VFT system configuration.

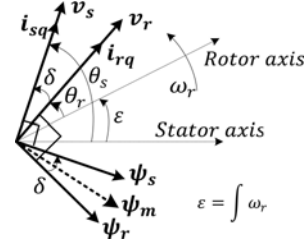


Fig. 2. Stator and rotor fluxes and voltages in VFT.

87 the fault propagation is a critical issue that affects power system
88 reliability and security, the FRT protection schemes should be
89 deployed in the VFT. In addition to that, the detailed control
90 strategy for VFT is not presented in the literature.

91 This paper presents a detailed hierarchical control strategy
92 for the VFT to achieve the following functions: establish a con-
93 nection between two power systems, power transfer control,
94 and FRT operation. Furthermore, a new topology of VFT com-
95 prising a series dynamic braking resistor (SDBR) is proposed
96 to enhance the FRT capability. A number of states are defined
97 for VFT operation to effectively connect it, operate it in steady
98 state, and protect it during the grid faults. The proposed control
99 strategy and VFT configuration are validated using real-time
100 hardware in-loop (HIL) simulation. The plant is simulated in
101 real time using OPAL-RT real-time simulator while the control
102 algorithm is implemented in dSPACE-1103 to carry out HIL
103 study.

104 II. VARIABLE FREQUENCY TRANSFORMER

105 Fig. 1 shows the VFT system configuration that consists of
106 a WRIM mechanically coupled with a dc motor drive. The
107 three-phase stator and rotor windings of WRIM are connected
108 to two asynchronous power networks namely power network-I
109 (PN-I) and power network-II (PN-II) as illustrated in Fig. 1. The
110 frequencies and/or phase angles of both PN-I (f_s and θ_s) and
111 PN-II (f_m and θ_m) could be different in actual application.

112 To connect the stationary VFT to the PN-I and PN-II sim-
113 ultaneously, the frequencies (f_s and f_m) and phase angles (θ_s and
114 θ_m) should be identical. It is difficult to achieve this condition in
115 practical system. Therefore, the following approach is deployed
116 with the VFT to make this asynchronous interconnection.

- 117 1) Connect the PN-I directly to the stator side of the VFT
118 (by closing CB1) while keeping the rotor stationary and
119 circuit breaker CB2 open.
- 120 2) Measure the frequency f_r and phase angle θ_r of the volt-
121 age induced in the rotor windings ($v_{r,abc}$) at the termi-
122 nals of CB2 (when the rotor is stationary, $f_r = f_s$ and
123 $\theta_r = \theta_s$).
- 124 3) Measure the frequency f_m and phase angle θ_m of PN-II
125 voltage ($v_{m,abc}$) available on the other side of CB2.
- 126 4) Control the rotor speed to change f_r by using the dc motor
127 drive to achieve $f_r = f_m$.
- 128 5) Adjust the rotor position (θ_r) using the dc motor drive to
129 make $\theta_r = \theta_m$.

- 6) The synchronization between voltages $v_{r,abc}$ and $v_{m,abc}$ is
130 achieved by steps 4 and 5, then the CB2 can be closed
131 to establish the interconnection between both networks
132 through VFT.
133

134 Here onwards, the points 4 and 5 are referred as frequency
135 matching and phase angle matching, respectively. A control
136 algorithm required to control the dc motor drive in VFT is
137 developed in Section V.

138 III. VFT CONCEPT AND POWER FLOW

139 Based on the existing literature, the working principle and
140 the active and reactive power flow through the VFT have not
141 been discussed in detail. In addition to that, FRT operation and
142 protection strategy have not been addressed. Hence, the detailed
143 VFT model is developed to study all the operational aspects for
144 steady-state, dynamic, and transient conditions.

145 A. Active Power Transfer and Control

146 The synchronization procedure described in the previous sec-
147 tion is used to connect both power networks in Fig. 1. Conse-
148 quently, both the stator and rotor fluxes will be in synchronism
149 irrespective of the rotor speed with a specific phase angle dif-
150 ference represented as load angle (δ). The controllability of this
151 load angle δ and its effect on active power transfer between both
152 networks is analyzed in this subsection.

153 The stator and rotor voltage vectors and the respective flux
154 vectors referred to stator are shown in Fig. 2. The instantaneous
155 stator flux (ψ_s), air-gap flux (ψ_m) and rotor flux (ψ_r) vectors
156 in the stationary reference frame can be expressed as

$$\psi_s = L_s \mathbf{i}_s + L_m (\mathbf{i}_r e^{j\varepsilon}) \quad (1)$$

$$\psi_m = L_m (\mathbf{i}_s + (\mathbf{i}_r e^{j\varepsilon})) \quad (2)$$

$$\psi_r = L_r \mathbf{i}_r + L_m (\mathbf{i}_s e^{-j\varepsilon}) \quad (3)$$

157 where L_s , L_r , and L_m represent the equivalent stator, rotor,
158 and mutual inductances referred to stator side; \mathbf{i}_s and \mathbf{i}_r are the
159 stator and rotor currents, respectively. ε is the angular displace-
160 ment between the stator and rotor fluxes and ω_r is the angular
161 (mechanical) speed of the rotor.

162 From Fig. 2 and (1)–(3), the expression for the electromag-
163 netic torque (T_e) can be obtained as [14]

$$T_e = \frac{2p}{3} \frac{L_m}{L_s L_r} \text{Im} [\psi_s \psi_r^*] = \frac{2p}{3} \frac{L_m}{L_s L_r} |\psi_s| |\psi_r^*| \sin \delta. \quad (4)$$

164 The aforementioned relationship shows that the electromag-
 165 netic torque developed is a cross product of stator and rotor
 166 fluxes, i.e., the product of magnitudes of ψ_s , ψ_r , and the sine
 167 of the angle δ between both the fluxes. On the other hand, gener-
 168 al expression for the developed electromagnetic torque in any
 169 reference frame (d - q or α - β) can be written as

$$T_e = k\psi_m i_q \quad (5)$$

170 where k is the torque constant, and i_q is component of current
 171 vector in quadrature with ψ_m . Here, the quadrature component
 172 of current refers to stator/rotor current as the angle between ψ_m
 173 and ψ_s or ψ_m and ψ_r is very small.

174 From the basic integral relation between the flux and volta-
 175 ge, a current that is in quadrature with the flux is in-phase or
 176 out-of-phase with the voltage and hence responsible for active
 177 power flow. In general, the VFT is connected between the two
 178 power systems whose voltages are fairly constant and hence the
 179 magnitudes of ψ_s , ψ_r , and ψ_m can be treated as constants.
 180 Therefore, from (4) and (5) it can be deduced that the torque
 181 developed/imposed on the rotor is proportional to 'Sin δ ' and active
 182 component of stator/rotor current. If the displacement angle
 183 ε in Fig. 2 is changed by applying external torque through the
 184 dc motor drive, the angle δ and hence electromagnetic torque
 185 developed in the WRIM will change according to (4). Conse-
 186 quently, it changes the active current (i_q) as per (5). It can be
 187 observed that the active current variation is in proportion to δ
 188 (as the δ is very small, $\text{Sin } \delta \approx \delta$), which is analogous to a series
 189 inductor behavior. The generalized active power flow through
 190 the series inductor is expressed by

$$P = \frac{V_s V_r}{X_s} \sin \delta. \quad (6)$$

191 Therefore, for the case of VFT, considering a stator to rotor
 192 turns ratio of 1:1, and neglecting the losses in the system, the
 193 active power transfer (P_{VFT}) in terms of the stator and rotor
 194 voltages, from Fig. 2, can be written as

$$P_{VFT} = \frac{V_s V_r}{X_s} \sin(\theta_s - (\theta_r + \varepsilon)) \quad (7)$$

195 where V_s and θ_s are the *rms* stator voltage and its phase angle,
 196 respectively; V_r and θ_r are the *rms* rotor voltage and its phase
 197 angle, respectively; and X_s is the series equivalent inductive
 198 reactance offered by the VFT. The term ε in (7) is the time
 199 integral of ω_r to be controlled by the dc motor drive.

200 By neglecting the leakage reactance and magnetizing current
 201 (i.e., power factors close to unity) of the VFT [2], the mechanical
 202 power handled by the dc motor drive can be expressed as

$$P_{dc} = P_s - P_r = V_s I_s - V_r I_r \quad (8)$$

203 where I_s and I_r are the *rms* values of the active component of sta-
 204 tor and rotor currents, respectively. Considering volt/hertz/turn
 205 and MMF balance between the stator and rotor windings of the
 206 VFT, the above expression can be rewritten as [2]

$$P_{dc} = V_s I_s - \left(\frac{V_s}{N_s f_s} N_r f_r \right) \left(\frac{I_s N_s}{N_r} \right) = V_s I_s \left(1 - \frac{f_r}{f_s} \right) \quad (9)$$

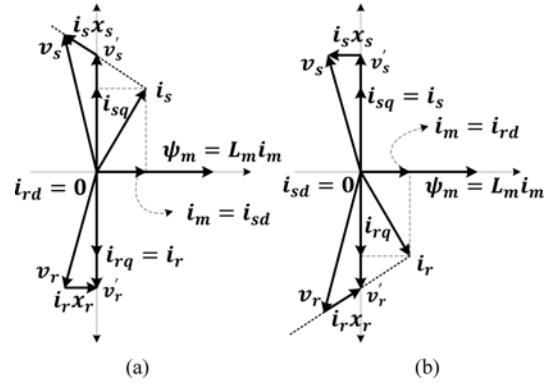


Fig. 3. Reactive power flow concept in the VFT. (a) $v_s > v_r$ (b) $v_s < v_r$

where N_s and N_r are the number of turns in the stator and 207
 rotor windings of VFT, respectively. From (9), it is clear that the 208
 power absorbed by the dc motor drive is a function of frequency 209
 difference between both the power networks and the power 210
 being transferred through the VFT. Also, from (9), the torque 211
 expression for the dc motor can be written as 212

$$T_{dc} = \frac{P_{dc}}{\omega_r} = \frac{V_s I_s \left(1 - \frac{f_r}{f_s} \right)}{2\pi \frac{120(f_s - f_r)/p}{60}} = \frac{p}{2} \frac{V_s I_s}{2\pi f_s} \quad (10)$$

where p is number of poles in the WRIM. From (10), it can 213
 be noticed that the torque developed by the dc motor drive is 214
 independent of speed of rotation. Assuming the constant stator 215
 voltage in (10), it can be noticed that by changing the torque 216
 applied through dc motor drive, the stator active current (I_s) 217
 can be changed. This proves the correlation between torque 218
 applied by dc motor drive and active current transferred through 219
 VFT according to (5). A simple armature voltage controlled 220
 four quadrant dc drive can be employed to regulate the torque 221
 produced by the dc motor and thereby active power transfer. 222

B. Reactive Power Transfer 223

Stator and rotor reactive currents (i_{sd} and i_{rd}) of VFT may 224
 consists of two components: 1) the magnetizing current required 225
 for VFT operation (i_m); and 2) the reactive current transferred 226
 between the two networks. The amount of reactive current suppl- 227
 ied/absorbed by each network is dependent on the voltage mag- 228
 nitudes at the stator (PCC-I) and rotor (PCC-II) terminals. 229
 Regardless of slight difference in grid voltages on both sides, 230
 the VFT maintains the volt/hertz/turn balance between induced 231
 stator (v'_s) and rotor (v'_r) voltages by circulating the appropriate 232
 amount of reactive current between both the networks. 233

Two different cases are demonstrated to show the reactive 234
 power flow dependency on the voltage magnitudes on both sides 235
 of VFT as illustrated in Fig. 3. The stator and rotor resistances 236
 are neglected and it is assumed that the active current transferred 237
 between the stator and rotor is constant ($i_{sq} = -i_{rq}$) throu- 238
 ghout the operation. Fig. 3(a) represents the case where the stator 239
 voltage is slightly higher than the rotor voltage referred to stator 240
 side (i.e., $v_s > v_r$). Assuming the induced stator voltage (v'_s) 241

is constant, any increase in v_s causes increase in i_s according to $v_s = v'_s + i_s x_s$. For the fixed active power transfer, active current (i_{sq}) is constant and hence reactive current (i_{sd}) has to increase in order to accommodate the change in i_s . In Fig. 3(a), the stator voltage magnitude is considered such that whole magnetizing current (i_m) required for VFT operation comes from the stator (i.e., $i_m = i_{sd}$ and $i_{rd} = 0$). Thus, further increase in the stator voltage magnitude leads to i_{sd} higher than i_m , that makes $i_{rd} = -(i_{sd} - i_m)$ which is the net reactive current transferred from PN-I to PN-II through VFT. Accordingly, any reduction in stator voltage magnitude drives the stator and rotor sides to supply the required magnetizing current i_m for VFT operation.

The vector diagram corresponding to the case where full magnetizing current is drawn from the rotor side due to higher rotor voltage is shown in Fig. 3(b). Similar to the aforementioned case, any further increase in the rotor voltage in Fig. 3(b) leads to reactive power flow from PN-II to PN-I.

It is obvious that the reactive power flow into/through VFT is uncontrolled and is mostly dependent on the terminal voltage magnitudes of v_s and v_r . The VFT requires a fixed amount of reactive power to meet the constant magnetization demand regardless of the amount and/or direction of active power transfer. The stator and rotor currents through VFT can be obtained from the steady-state equivalent circuit for particular voltage conditions and reactive powers can be computed as

$$Q_s = |\nu_s| |i_{sd}| = \text{Im} [\nu_s i_s^*] \quad (11)$$

$$Q_r = |\nu_r| |i_{rd}| = \text{Im} [\nu_r i_r^*]. \quad (12)$$

For the power flow directions shown in Fig. 1, the reactive power absorbed by VFT (Q_m) at any operating condition is the difference between stator and rotor reactive powers, i.e.,

$$Q_m = Q_s - Q_r. \quad (13)$$

IV. SDBR PROTECTION SCHEME FOR VFT

As discussed in the previous section, during the steady-state operation, VFT is analogous to a series inductor. Therefore, during a voltage dip resulted from the grid fault in one of the power networks, the other network is forced to supply a large fault currents. This indicates the propagation of a fault from the faulted network to the healthy power network through VFT. This fault propagation phenomenon associated with VFT has not been discussed in the literature. To demonstrate the problems associated with the fault propagation, a fault condition is considered at PN-II as shown in Fig. 1. This grid fault (or voltage dip) has the following consequences unless appropriate protective measures are taken:

- 1) large fault currents from the stator side;
- 2) temporary disconnection of VFT due to CB1 opening;
- 3) oscillations/instability in PN-I due to system dynamics;
- 4) slow post fault recovery due to VFT disconnection;
- 5) possible requirement of VFT resynchronization;
- 6) damage to VFT windings in the event of protection failure.

This paper introduces an appropriate FRT scheme within the VFT system using SDBR to overcome the issue of fault propagation as shown in Fig. 4. The SDBR protection scheme is

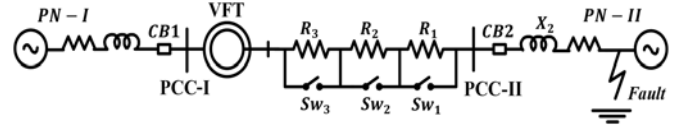


Fig. 4. Single line diagram of SDBR protection scheme for VFT.

identified as simple and economic solution for enhancing the FRT capability and transient performance of VFT in response to symmetrical and asymmetrical grid faults. It can be noted that, four different combinations of power flow direction (PN-I to PN-II or PN-II to PN-I) and the grid fault (in PN-I or PN-II) are possible in the VFT. The SDBR scheme that can prevent the fault propagation in all four possible cases can be designed using a simple approach by considering a power flow from PN-I to PN-II and the grid fault in PN-II as described in the following.

A. Series Resistance Selection

According to the design criteria, the SDBR should limit the fault current by acting as a voltage booster against the voltage in PN-II at the rotor terminals and protect the healthy network (PN-I) connected to the stator terminal. To be able to work with various levels of grid faults (based on magnitudes of voltage dip), the SDBR should have different combination of resistors. The SDBR with n resistors can realize $(2^n - 1)$ combinations of resistances. The maximum and minimum possible resistance values of SDBR should be selected based on the following two scenarios.

1) *Voltage Dip Operation*: During the most severe grid fault, the voltage appears on the rotor terminals should be higher than the minimum allowable rotor voltage (V_{r_min}). The maximum value of series resistance ($R_{SDBR_max} = R_1 + R_2 + \dots + R_n$) required to achieve this during the worst case voltage dip can be calculated using the following:

$$V_{\text{fault_min}} + \frac{P_{\text{rated}}}{3V_{r_min}} R_{SDBR_max} \geq kV_{r_min} \quad (14)$$

where $V_{\text{fault_min}}$ is the lowest possible grid voltage (at PCC-II) during the grid fault on PN-II, P_{rated} is the rated power transfer capability of VFT, and k is safety margin (>1) to take care of the lagging power factor.

2) *Overvoltage Protection*: The designed SDBR should not cause the overvoltage across the rotor terminals in any case such as small voltage dips. The minimum value of series resistance (R_{SDBR_min}) that prevents the rotor overvoltage can be computed from the following equation:

$$V_{\text{fault_max}} + \frac{P_{\text{rated}}}{3V_{r_rated}} R_{SDBR_min} \leq 3V_{r_rated} \quad (15)$$

where $V_{\text{fault_max}}$ is the grid voltage (at PCC-II) during the minor voltage dip that can trigger the SDBR. For the present case of SDBR with three resistances, the value of different resistors can be calculated from the maximum and minimum values of

331 SDBR resistances obtained through (14) and (15) as follows:

$$\begin{aligned}
 R_1 &= R_{\text{SDBR_min}} \\
 R_2 &= \frac{1}{3} [R_{\text{SDBR_max}} - R_{\text{SDBR_min}}] \\
 R_3 &= \frac{2}{3} [R_{\text{SDBR_max}} - R_{\text{SDBR_min}}].
 \end{aligned} \quad (16)$$

332 B. Static AC Switch Selection

333 Three SDBR resistors can be inserted into the circuit by controlling the static ac switches Sw_1 , Sw_2 , and Sw_3 , respectively. Three ac switches are required for switching the resistors (R_1 , R_2 , and R_3) in each phase as per Fig. 4. Therefore, a total of nine resistors (R_1 , R_2 , and R_3 for each phase) and nine ac switches are deployed to realize the SDBR protection scheme.

339 The current rating of ac switches in SDBR scheme should be equal to the rated VFT current as they remain closed during the steady-state operation. And, the voltage rating of the switches should be equal to the product of rated VFT current and corresponding resistor value. It is worthy to note that the switching losses are absent (as switches are always closed) during the steady-state operation and therefore, the switches with low conduction losses are preferred for this SDBR scheme.

347 The ac switches can be realized using either antiparallel thyristors (low cost) or antiserries IGBTs (high cost). The choice of the switch depends on the speed requirement of resistor insertion during the fault. The antiparallel thyristor switch has a maximum of half cycle delay in operation as it breaks the current at next zero crossing while, antiserries IGBT switch can break the current instantaneously.

354 The WRIM in the VFT system possesses large thermal time constant and can easily handle the current surge resulted from the delay in ac switch opening. Therefore, the low cost antiparallel thyristor switches are used as ac switches in SDBR protection scheme.

359 V. PROPOSED HIERARCHICAL CONTROL STRATEGY

360 This section describes the overall control of VFT and SDBR. The dc motor drive is the only controllable device in a VFT system that can regulate the power flow between two power networks. However, as highlighted in the previous section SDBR is an additional controllable device for the restriction of fault propagation. A comprehensive hierarchical strategy, with all the necessary controls, is proposed in three operational stages.

367 When the stator is directly connected to PN-I and circuit breaker CB2 is open, the dc motor drive is to be controlled to achieve the frequency matching ($f_r = f_m$) and phase angle matching ($\theta_r = \theta_m$). This part of control is realized in first two stages (Stage-I and Stage-II) of the proposed hierarchical control. Once the connection is established between both the power networks through VFT, the power transfer control is carried out in Stage-III.

375 The control block diagram depicting these three stages of the proposed hierarchical control is shown in Fig. 5. A four-quadrant armature voltage control method is employed for dc drive in the proposed hierarchical control. The changeover from

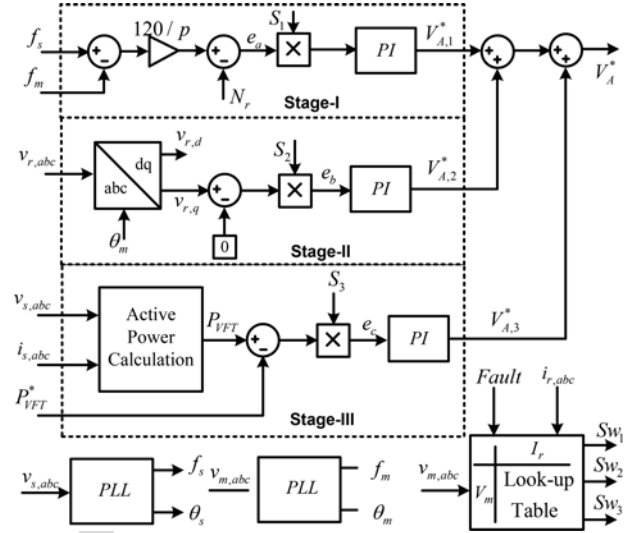


Fig. 5. Proposed hierarchical control strategy for synchronization and power transfer control in VFT.

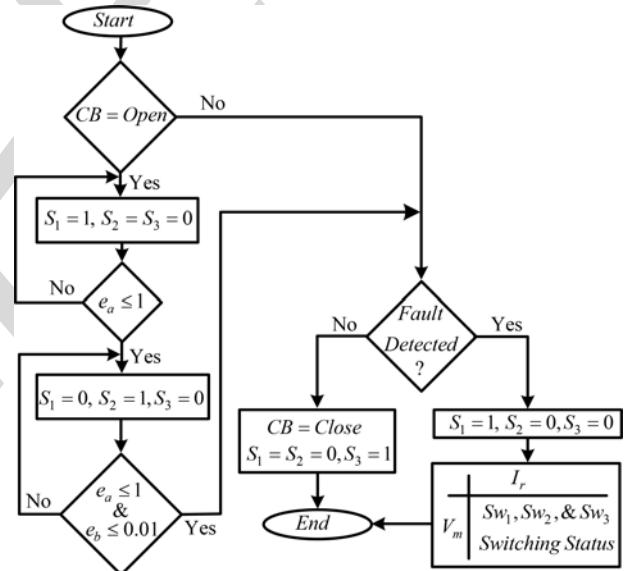


Fig. 6. Flow chart for hierarchical control strategy and SDBR control.

one stage to another is realized using the states S_1 , S_2 , and S_3 as illustrated in Fig. 5 with the predefined hierarchy depicted in Fig. 6. The control of SDBR protection scheme is also incorporated in the flow chart of Fig. 6. The objective and control of VFT in each stage of hierarchical control is discussed in the following subsections.

A. Stage-I: Frequency Matching

Initially when the stator of WRIM is connected to PN-I, the rotor is stationary and CB2 is open, the command $S_1 = 1$ is issued to start the frequency matching stage. At this condition the frequency of rotor voltage f_r has to be changed from $f_r = f_s$ to $f_r = f_m$. To achieve this desired frequency change, the equivalent rotor speed at which the rotor of VFT should be

392 driven by dc motor drive is

$$N_r^* = \frac{120(f_s - f_m)}{p}. \quad (17)$$

393 The reference (N_r^*) and actual (N_r) speeds are compared,
 394 and the error, e_a , is processed through the PI controller to gen-
 395 erate the necessary armature voltage ($V_{A,1}^*$) for the armature
 396 controlled dc motor drive (shown in Stage-I of Fig. 5). Once,
 397 the mean of absolute speed error (e_a) goes below 1 r/min, S_1
 398 becomes low and S_2 becomes high as shown in the flow chart
 399 given in Fig. 6. Thereafter, high state of S_2 enables the next
 400 stage of hierarchical control.

401 B. Stage-II: Phase Angle Matching

402 Subsequent to the frequency matching, the next objective is
 403 to achieve the phase angle matching between $v_{r,abc}$ and $v_{m,abc}$
 404 (i.e., $\theta_r = \theta_m$). Applying $abc-dq$ transformation on the mea-
 405 sured rotor voltages ($v_{r,abc}$) using the phase angle (θ_m) of PN-II
 406 voltage ($v_{m,abc}$), obtained from the phase locked loop (PLL),
 407 gives the direct ($v_{r,d}$) and quadrature ($v_{r,q}$) components of rotor
 408 voltages referred to PN-II voltage phasor. When the rotor volt-
 409 age phase angle (θ_r) is exactly equal to θ_m , the computed $v_{r,q}$
 410 becomes zero. In other words, by making $v_{r,q} = 0$, the phase
 411 angles can be matched (θ_r and θ_m). To achieve this, a PI con-
 412 troller is used over the $v_{r,q}$ for generating the necessary armature
 413 voltage ($V_{A,2}^*$) to change the rotor position (shown in Stage-II
 414 of Fig. 5). As soon as the mean of the absolute phase angle error
 415 (e_b or $v_{r,q}$) goes below certain margin (say 1%), S_2 goes low
 416 indicating the completion of Stage-II (shown in Fig. 6).

417 After frequency and phase angle matching are completed,
 418 the CB2 closes to establish the connection between both the
 419 networks through VFT. Subsequently, S_3 goes high to enable
 420 the power transfer controller.

421 C. Stage-III: Power Transfer Control

422 Actual power transfer (P_{VFT}) from PN-I to PN-II is measured
 423 on the stator side of VFT and compared with the reference
 424 power (P_{VFT}^*). The error is passed through the PI controller
 425 to generate the necessary armature voltage ($V_{A,3}^*$) and thus to
 426 control the torque developed by the dc motor drive (T_{dc}). The
 427 torque produced by dc motor drive dynamically adjusts the angle
 428 ε to achieve the desired load angle δ that makes $P_{VFT}^* = P_{VFT}$
 429 as per (7).

430 The reference armature voltage (V_A^*) for the dc motor drive
 431 is expressed as follows:

$$V_A^* = V_{A,1}^* + V_{A,2}^* + V_{A,3}^*. \quad (18)$$

432 During the power transfer control, any change in the networks
 433 frequencies forces the rotor to adjust its speed according to (17).

434 D. SDBR-Based Fault Ride-Through Control

435 The SDBR control and fault detection is integrated in the hier-
 436 archical control strategy as shown in Fig. 6. When the grid fault
 437 occurs, the power transfer control should saturate at its prefault
 438 value to avoid rotor acceleration in response to fault conditions.
 439 This is achieved by forcing $S_3 = 0$ to keep the corresponding

PI controller output at its prefault value. Whereas, the command
 $S_1 = 1$ (frequency matching loop) is reissued during the fault
 to damp out the rotor oscillations by controlling the torque of
 the dc motor drive. Simultaneously, there is a need to insert a
 suitable combination of resistors in SDBR that prevent the fault
 propagation from the faulted network to the healthy network.
 This is obtained using a two-dimensional (2 D) lookup table
 based on VFT current and fault voltage magnitudes. The out-
 put of lookup table is status of switches S_{w1} , S_{w2} , and S_{w3}
 that inserts an appropriate combination of R_1 , R_2 , and R_3 . The
 switches S_{w1} , S_{w2} , and S_{w3} of each phase are simultaneously
 controlled for balanced faults while they are controlled inde-
 pendently for each phase during the unbalance faults. After the
 fault is cleared, the power transfer controller is reactivated to
 maintain the power transfer control by giving the control sig-
 nals $S_1 = S_2 = 0$, $S_3 = 1$. The coordination between the three
 stages of the proposed hierarchical control and the proposed
 SDBR control is shown in Fig. 6.

458 VI. REAL-TIME HARDWARE IN-LOOP VALIDATION

459 The proposed hierarchical control strategy and SDBR scheme
 460 for VFT are verified using a real-time HIL implementation. The
 461 control algorithm is implemented in the digital signal processor
 462 (DSP) board, DS1103 from dSPACE at a step size of 50 μ s. The
 463 plant (VFT test system and SDBR scheme) is emulated using
 464 the OPAL-RT real-time simulator. The communication between
 465 the controller and the plant is carried out through ADC and DAC
 466 ports of DS1103 and OPAL-RT.

467 Due to high torque requirement by the VFT system during
 468 low speed operations, a geared dc motor with a mechanical gear
 469 of ratio 1:10 is used instead of conventional dc motor. The use
 470 of geared dc motors can significantly reduce the size of the
 471 dc motor during the actual applications of VFT. The system
 472 specifications and the machine parameters of VFT test system
 473 are given in Table I.

474 A. Steady-State Performance

475 The performance of VFT system during the three stages of
 476 proposed hierarchical control is shown in Figs. 7–9. All the re-
 477 sults are given in per unit values with 1 div = 1 p.u. The dc
 478 motor drive power P_{dc} and speed N_r are represented on the
 479 basis of 100 W and 60 r/min for a better visualization of their
 480 dynamics. The PN-I operates at 400 V/50 Hz while the PN-II
 481 operates at 392 V/49 Hz. The effectiveness of each stage of hier-
 482 archical control and the transition from one stage to another can
 483 be seen from Fig. 7. When VFT is stationary the frequency f_r
 484 of the induced rotor voltage ($v_{r,a}$) is 50 Hz while the frequency
 485 f_m of PN-II voltage ($v_{m,a}$) is 49 Hz. As highlighted in Section
 486 II, to close the circuit breaker CB2, synchronization should be
 487 established between the $v_{r,a}$ and $v_{m,a}$. Therefore in Stage-I,
 488 with the frequency matching command $S_1 = 1$, the rotor speed
 489 N_r is controlled to change f_r such that $f_r = f_m$. By the end
 490 of Stage-I (just before t_1), the frequency of $v_{r,a}$ is achieved
 491 equal to 49 Hz by regulating the VFT rotor speed at 0.5 p.u.
 492 (30 r/min) as per (17). Subsequent to successful completion of
 493 Stage-I at t_1 , the status of commands S_1 and S_2 automatically

TABLE I
 SYSTEM SPECIFICATIONS

WRIM specifications and parameters	
Power network-I	400 V, 50 Hz
Power network-I series inductance	0.03 p.u.
Power network-II	392 V, 49 Hz
Power network-II series inductance	0.052 p.u.
WRIM specifications and parameters	
Rated apparent power	4150 VA
Rated active power	3500 W
Rated voltage and frequency	400 V, 50 Hz
Number of poles	4
Stator to rotor turns ratio	400/400
Stator resistance	0.01965 p.u.
Stator inductance	0.0397 p.u.
Rotor resistance referred to stator	0.01965 p.u.
Rotor inductance referred to stator	0.0397 p.u.
Magnetizing (mutual) inductance	1.354 p.u.
Inertia constant	0.09526 s
DC motor drive specifications	
Rated output power	500 W
Rated armature voltage	500 V
Rated field voltage	300 V
Number of poles	4
Mechanical gear ratio	1/10
Electrical connection of dc drive	To power network-I

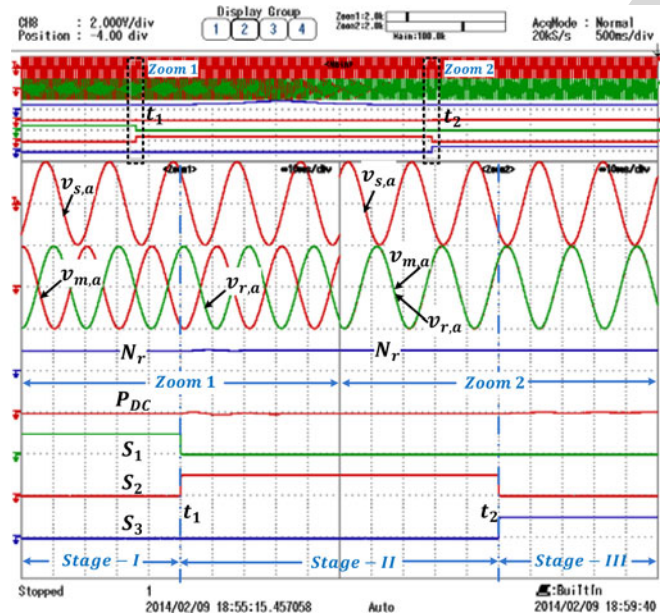


Fig. 7. Different stages in the proposed hierarchical control.

494 changes to $S_1 = 0$ and $S_2 = 1$ (Zoom1). In Stage-II, the phase
 495 angle matching of $v_{r,a}$ and $v_{m,a}$ is performed. To match the
 496 phase angles of both the voltages by changing the instantaneous
 497 rotor position of VFT, the speed of dc motor drive temporarily
 498 deviates from its reference speed. This operation can be seen
 499 from the temporary variations in N_r and the power handled by
 500 the dc drive (P_{dc}). The successful matching of frequencies and
 501 phase angles of $v_{r,a}$ and $v_{m,a}$ can be observed from Zoom2
 502 (just before time t_2). Stage-II ends at t_2 where the status of
 503 commands S_2 and S_3 are changed to $S_2 = 0$ and $S_1 = 1$ and

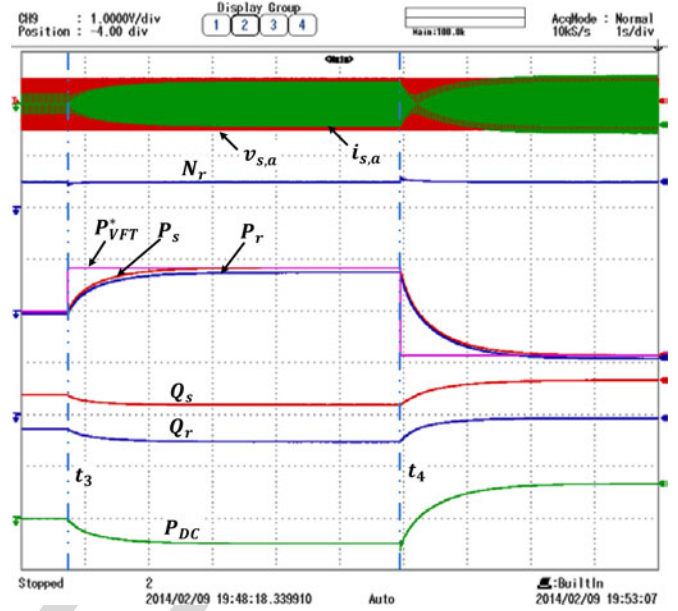


Fig. 8. Power control using the hierarchical control (dynamic performance).

the circuit breaker CB2 is closed to initiate the power transfer
 stage (Stage-III).

The performance of VFT during Stage-III is depicted in
 Figs. 8 and 9. According to power flow directions considered in
 Fig. 1, the positive value of P_{VFT}^* represents the power trans-
 ferred from PN-I (stator side) to PN-II (rotor side) and negative
 quantity represents the reverse power flow.

The dynamic response of VFT during sudden changes in
 power transfer command (P_{VFT}^*) is shown in Fig. 8. Initially,
 P_{VFT}^* is set equal to zero, and at t_3 , it is changed from 0 to
 0.85 p.u. It can be noticed that P_s and P_r reach the steady state
 ($P_s = P_{VFT}^*$) within 3 s. Further to check the response of VFT
 during power reversal, P_{VFT}^* is changed from 0.85 to -0.85
 p.u. at t_4 . It can be observed that VFT reaches the new steady
 state within 3 s in this case as well. Note that, due to the active
 power loss in VFT there is a small difference between P_s and
 P_r during the steady state. The active power supplied/absorbed
 by the dc drive is governed by the direction of power transfer
 and it is observed around 0.5–0.7 p.u. (around 0.012–0.015 p.u.
 on VFT power base).

The expanded view of steady-state results for P_{VFT}^* equal to
 0.85 and -0.85 p.u. is shown in Fig. 9 in Zoom1 and Zoom2,
 respectively. In Zoom1, it can be noticed that the stator current
 $i_{s,a}$ is nearly in-phase with stator voltage $v_{s,a}$ as the power
 is being transferred from PN-I to PN-II. Whereas in case of
 reverse power flow (Zoom2), $i_{s,a}$ is noticed to be almost out-of-
 phase with $v_{s,a}$. The change in Q_s and Q_r with the change in
 P_{VFT}^* (in Figs. 8 and 9) represents their uncontrolled nature as
 discussed in Section III-B. Due to this, the stator current ($i_{s,a}$)
 magnitudes are different for the same amount of active power
 flow in both directions. Note that the difference between Q_s
 and Q_r is almost constant as per (13) and is equal to the reactive
 power absorbed/required by VFT (Q_m).

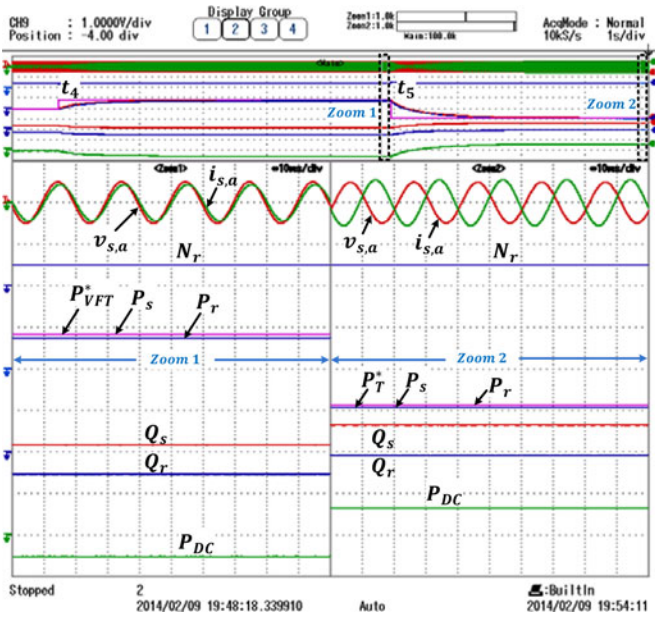


Fig. 9. Power control using the hierarchical control (steady-state performance).

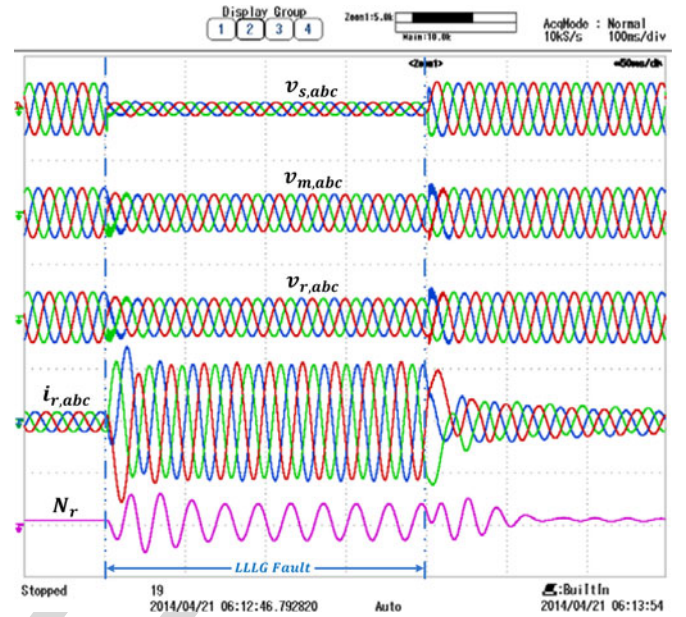


Fig. 11. VFT performance during three-phase fault in PN-I (stator side) without SDBR protection scheme.

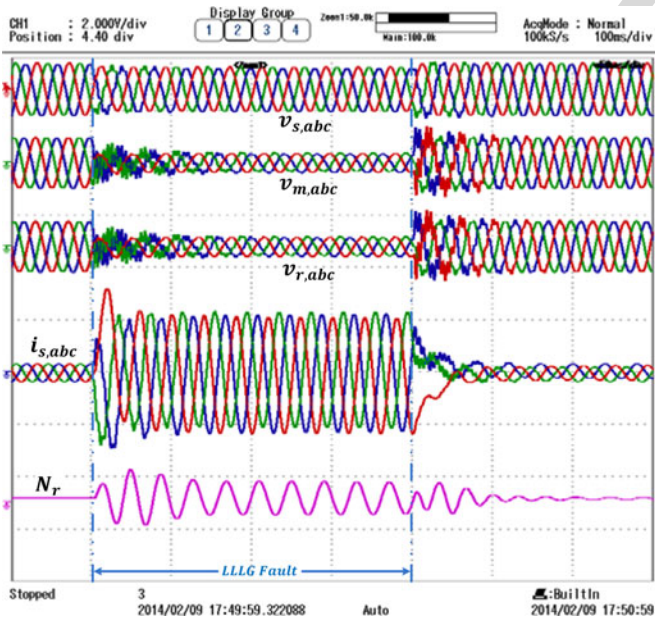


Fig. 10. VFT performance during three-phase fault in PN-II (rotor side) without SDBR protection scheme.

537 B. Fault Ride-Through Performance

538 The behavior of VFT without any additional FRT mechanism,
 539 during the three-phase grid fault at PN-II is shown in Fig. 10.
 540 The important variables that depict the fault propagation problem
 541 with VFT are shown in Fig. 10. These variables include:
 542 PN-I voltage at PCC-I ($v_{s,abc}$: 1 div = 2 p.u.), the
 543 PN-II voltage at PCC-II ($v_{m,abc}$: 1 div = 2 p.u.), the rotor
 544 voltage ($v_{r,abc}$: 1 div = 2 p.u.), current drawn from PN-I
 545 ($i_{s,abc}$: 1 div = 5 p.u.), and the rotor speed (N_r : 1 div = 5

p.u.). Prior to the grid fault, the system is under steady state
 546 with a power transfer of 0.85 p.u. from PN-I to PN-II. A
 547 significant voltage dip in both PCC-II ($v_{m,abc}$) and rotor ($v_{r,abc}$)
 548 voltages and sudden rise in stator current ($i_{s,abc}$) can be noticed
 549 during the grid fault condition. The rise in stator current signi-
 550 fies that the fault in the rotor side (PN-II) is propagated to the
 551 stator side (PN-I). The fault current in PN-I reaches 5 p.u. which
 552 may cause threat to PN-I security and reliability. Moreover, the
 553 large oscillations introduced in the rotor speed (N_r) during the
 554 grid fault causes the sustained mechanical vibrations that may
 555 destroy the WRIM and dc motor bearings.
 556

The fault propagation from the stator side to rotor side during
 557 a grid fault on stator side (PN-I) is depicted in Fig. 11. It can
 558 be noticed that the rotor current rises 5 p.u. during the fault without
 559 SDBR protection. This signifies the fault propagation from PN-I
 560 to PN-II.
 561

To avoid such high fault currents and mechanical stress due to
 562 fault propagation, the SDBR protection scheme shown in Fig. 4
 563 is designed (explained in Section III). The set of specifications
 564 considered during the SDBR design are: $V_{\text{fault_min}} = 0.1$ pu,
 565 $V_{\text{fault_max}} = 0.9$ pu, $P_{\text{rated}} = 0.85$ p.u., $k = 1.1$ and $V_{r_min} =$
 566 0.9 pu. The values for $R_{\text{SDBR_max}}$ and $R_{\text{SDBR_min}}$ calculated
 567 using (14) and (15) are 4Ω and 40Ω , respectively. From (16), the
 568 SDBR resistance values computed are $R_1 = 4 \Omega$, $R_2 = 12 \Omega$,
 569 and $R_3 = 24 \Omega$ respectively.
 570

The performance of VFT with the proposed SDBR scheme
 571 during three-phase to ground fault on PN-II is shown in Fig. 12.
 572 Due to the activation of SDBR scheme during the three-phase
 573 fault, the rotor voltage ($v_{r,abc}$) is restored to the nominal level
 574 and the stator current ($i_{s,abc}$) is restricted to the maximum rated
 575 current. As the activation of SDBR does not allow the stator
 576 current to reach high value, it prevents the fault propagation
 577 through VFT. The oscillations in the speed are also reduced with
 578

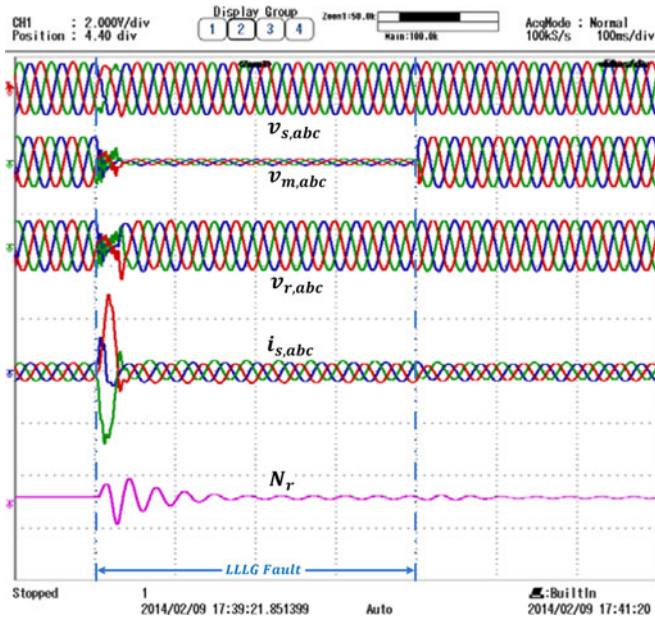


Fig. 12. VFT performance during three-phase fault in PN-II (rotor side) with the SDBR protection scheme.

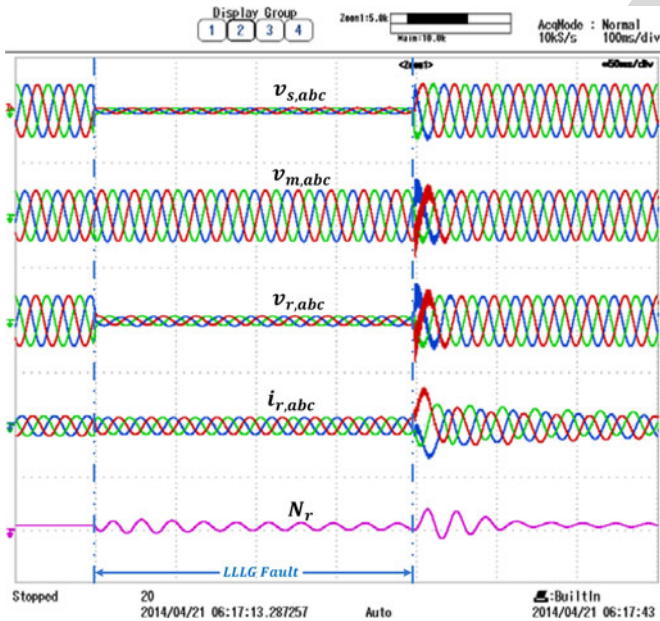


Fig. 13. VFT performance during three-phase fault in PN-I (stator side) with the SDBR protection scheme.

579 the SDBR and are damped out due to the presence of mechanical
580 inertia and opposing torque produced by the dc motor drive.

581 The performance of VFT with the proposed SDBR protec-
582 tion scheme during the three-phase to ground fault on the stator
583 side (PN-I) is depicted in Fig. 13. It can be observed that the
584 grid fault on the stator side causes a sudden dip in stator vol-
585 age, $v_{s,abc}$. During this condition, the insertion of SDBR series
586 resistance on the rotor side brings down the $v_{r,abc}$ without
587 affecting $v_{m,abc}$. This restricts the flow of fault current through

VFT to a nominal level as noticed from $i_{r,abc}$. Note that the rise
588 in $i_{r,abc}$ immediately after the fault clearance is mainly due to
589 the sudden change in stator flux caused by the abrupt recovery
590 of stator voltage.
591

The satisfactory performance during the steady-state, dyn-
592 amic, and grid fault conditions proves that VFT with proposed
593 SDBR scheme and hierarchical control strategy is a potential
594 contender for the application of controlled power transfer be-
595 tween two asynchronous power networks.
596

VII. CONCLUSION

This paper presents a new hierarchical control strategy to
598 control the VFT during normal and FRT operating conditions.
599 This paper further investigates the possible fault propagation
600 issue through VFT from one network to another. The SDBR-
601 based FRT scheme has been proposed for VFT to mitigate the
602 fault propagation. The detailed working principles of the VFT,
603 all the stages of hierarchical control and FRT operation are
604 verified using the real-time HIL system.
605

The detailed results under three stages of the proposed hier-
606 archical control (frequency matching, phase angle matching, and
607 power transfer control) during steady-state and dynamic condi-
608 tions prove its comprehensiveness. The satisfactory results in
609 limiting the fault propagation through VFT during the grid faults
610 validate the effectiveness of SDBR protection scheme. In sum-
611 mary, along with the power transfer control function of VFT,
612 added capability to limit the fault propagation and inherent nat-
613 ural damping capability will make VFT an ideal solution for the
614 interconnection of micro grids in the future power systems.
615

REFERENCES

- [1] M. P. Bahrman, "Overview of HVDC transmission," in *Proc. Power Syst. Conf. Expo.*, 2006, pp. 18–23. 617
- [2] A. Merkhof, P. Doyon, and S. Uphadayay, "Variable frequency transformer—Concept and electromagnetic design evaluation," *IEEE Trans. Energy Convers.*, vol. 23, no. 4, pp. 989–996, Dec. 2008. 618
- [3] E. Larsen, "A classical approach to constructing a power flow controller," in *Proc. IEEE Power Eng. Soc. Summer Meeting*, 1999, vol. 2, pp. 1192–1195. 619
- [4] R. J. Piwko, E. V. Larsen, and C. A. Wegner, "Variable frequency transformer—a new alternative for asynchronous power transfer" in *Proc. IEEE Power Eng. Soc. Conf. Expo.*, Durban, Jul. 2005, pp. 393–398. 620
- [5] B. Bagen, D. Jacobson, G. Lane, and H. M. Turanli, "Evaluation of the performance of back-to-back HVDC converter and variable frequency transformer for power flow control in a weak interconnection," presented at IEEE Power Eng. Soc. Gen. Meeting, Tampa, FL, USA, Jun. 24–28, 2007, pp. 1–6. 621
- [6] A. S. Abdel-Khalik, A. Elserougi, S. Ahmed, and A. Massoud, "Brushless doubly fed induction machine as a variable frequency transformer," in *Proc. 6th IET Int. Conf. Power Electron., Mach. Drives*, Mar. 2012. 622
- [7] A. H. El Din, M. A. Abdullah, and M. Ibrahim, "A Matlab/Simulink model to study the performance of the VFT for the interconnection of weak and strong AC grids," in *Proc. IEEE Int. Elect. Mach. Drives Conf.*, May 2011, pp. 1635–1640. 623
- [8] E. T. Raslan, A. S. Abdel-Khalik, M. Abdulla, and M. Z. Mustafa, "Performance of VFT when connecting two power grids operating under different frequencies," in *Proc. 5th IET Int. Conf. Power Electron., Mach. Drives*, 19–21, Apr. 2010, pp. 1–6. 624
- [9] G. Chen and X. Zhou, "Digital simulation of variable frequency transformers for asynchronous interconnection in power system," in *Proc. IEEE Power Eng. Soc. Transmiss. Distrib. Conf.*, 2005, pp. 1–6. 625

- 647 [10] L. Contreras-Aguilar and N. Garcia, "Accelerated time domain solution of VFT using the Poincaré map method with an embedded implicit integration algorithm" in *Proc. North Am. Power Symp.*, Calgary, Canada Sep. 2008, pp. 1–8.
- 648
649
650
- 651 [11] L. Contreras-Aguilar and N. Garcia, "Fast convergence to the steady state operating point of a VFT park using the limit cycle method and a reduced order model," in *Proc. IEEE Power Eng. Soc. Gen. Meeting*, Calgary, Canada, Jul. 2009, pp. 1–5.
- 652
653
654
- 655 [12] L. Contreras-Aguilar and N. Garcia, "Steady-state solution of a VFT park using the Newton method and a reduced order model," in *Proc. IEEE Power Tech.*, Bucharest, Rumania, Jun./Jul. 2009, pp. 1–6.
- 656
657
- 658 [13] L. Wang and L. Y. Chen, "Reduction of power fluctuations of a large scale grid-connected offshore wind farm using a variable frequency transformer," *IEEE Trans. Sustain. Energy*, vol. 2, no. 3, pp. 226–234, Jul. 2011.
- 659
660
661
- 662 [14] G. Poddar and V. T. Ranganathan, "Direct torque and frequency control of double-inverter-fed slip-ring induction motor drive," *IEEE Trans. Ind. Electron.*, vol. 51, no. 6, pp. 1329–1337, Dec. 2004.
- 663
664
- 665 [15] P. Marken, J. Roedel, D. Nadeau, D. Wallace, and H. Mongeau, "VFT maintenance and operating performance," in *Proc. Power Eng. Soc. Gen. Meeting Convers. Del. Elect. Energy*, Jul. 2008, pp. 1–5.
- 666
667
- 668 [16] D. Nadeau, "A 100-MW variable frequency transformer (VFT) on the Hydro-Quebec TransEnergie Network—the behavior during disturbance" in *Proc. Power Eng. Soc. Gen. Meeting*, Jun. 2007, pp. 1–5.
- 669
670



Bharath Babu Ambati received the B.E. degree in electrical and electronics engineering from the Sir C. R. Reddy College of Engineering (affiliated with Andhra University), Eluru, AP, India, in 2009; the M.Tech. degree in power electronics, electrical machines, and drives (PEEMD) from the Indian Institute of Technology (IIT) Delhi, New Delhi, India, in 2011; and is currently pursuing the Ph.D. degree in interdisciplinary engineering with the Masdar Institute of Science and Technology, Abu Dhabi, UAE.

From 2011 to 2012, he was with Schneider Electric India Private Limited as a Product Expert of Motion and Drives. His current research interests include power electronics, electrical machines, renewable energy generation, and power quality.



Parag Kanjiya received the B.Eng. degree in electrical engineering from the B.V.M. Engineering College, Sardar Patel University, V.V. Nagar, India, in 2009, and the M.Tech. degree in power systems from the Indian Institute of Technology Delhi (IITD), New Delhi, India, in 2011.

Since October 2011, he has been a Research Engineer with the Masdar Institute of Science and Technology, Abu Dhabi, UAE. His research interests include applications of power electronics in distribution systems, power quality enhancement, renewable energy, FACTS, and power system optimization.

Mr. Kanjiya was awarded the K.S. Prakasa Rao Memorial Award for earning the highest C.G.P.A at IITD in August, 2011.



Vinod Khadkikar (S'06–M'09) received the B.E. degree from the Government College of Engineering, Dr. Babasaheb Ambedkar Marathwada University, Aurangabad, India, in 2000; the M. Tech. degree from the Indian Institute of Technology (IITD), New Delhi, India, in 2002; and the Ph.D. degree from the École de Technologie Supérieure (ETS), Montréal, QC, Canada, in 2008, all in electrical engineering.

From December 2008 to March 2010, he was a Post-Doctoral Fellow at the University of Western Ontario, London, ON, Canada. From April 2010 to December 2010, he was visiting faculty at the Massachusetts Institute of Technology, Cambridge, MA, USA. Currently, he is an Associate Professor at the Masdar Institute of Science and Technology, Abu Dhabi, UAE. His research interests include applications of power electronics in distribution systems and renewable energy resources, grid interconnection issues, power quality enhancement, active power filters, and electric vehicles.

Dr. Khadkikar is currently an Associate Editor of the *IET Power Electronics Journal*.



Mohamed Shawky El Moursi (M'12) received the B.Sc. and M.Sc. degrees from Mansoura University, Mansoura, Egypt, in 1997 and 2002, respectively, and the Ph.D. degree from the University of New Brunswick (UNB), Fredericton, NB, Canada, in 2005, all in electrical engineering.

He was a Research and Teaching Assistant in the Department of Electrical and Computer Engineering, UNB, from 2002 to 2005. He joined McGill University as a Post-Doctoral Fellow with the Power Electronics Group. He joined Vestas Wind Systems, Arhus, Denmark, in the Technology R&D Group with the Wind Power Plant Group. He was with TRANSCO, UAE, as a Senior Study and Planning Engineer, and seconded as a Faculty Member in the Faculty of Engineering, Mansoura University. He was a Visiting Professor at the Massachusetts Institute of Technology, Cambridge, MA, USA. He is currently an Associate Professor in the Electrical Engineering and Computer Science Department, Masdar Institute of Science and Technology. His research interests include power system, power electronics, FACTS technologies, system control, wind turbine modeling, wind energy integration, and interconnections.

He is serving as an Associate Editor for *IET Renewable Power Generation* and *IET Power Electronics Journals*.



James L. Kirtley Jr. (F'91) received the Ph.D. degree from the Massachusetts Institute of Technology (MIT), Cambridge, MA, USA, in 1971.

He has been with the Large Steam Turbine Generator Department General Electric, and with Satcon Technology Corporation. Currently, he is a Professor of Electrical Engineering at MIT.

Dr. Kirtley served as an Editor-in-Chief of the IEEE TRANSACTIONS ON ENERGY CONVERSION from 1998 to 2006, and continues to serve as Editor and as a Member of the Editorial Board of *Electric Power Components and Systems*. He was awarded the IEEE Third Millennium Medal in 2000 and the Nikola Tesla Prize in 2002. He is a Registered Professional Engineer in Massachusetts and is a member of the United States National Academy of Engineering.

671
672
673
674
675
676
677
678
679
680
681
682
683
684
685

686
687
688
689
690
691
692
693
694
695
696
697
698
699
700

Q5

Q6

Q7

Q8

759

QUERIES

Q1. Author: Please spell out of OPAL-RT, PID, FACTS and C.G.P.A.	760
Q2. Author: Please check whether the edit in the sentence starting: “The dc motor drive power . . .” is ok.	761
Q3. Author: Please provide page range in Ref. [6].	762
Q4. Author: Please provide location details.	763
Q5. Author: Please check if the edits to the BIOS of author “Vinod Khadkikar” are ok.	764
Q6. Author: Please provide location details.	765
Q7. Author: Please provide field of study.	766
Q8. Author: Please provide location details.	767
	768

IEEE
Proof

A Hierarchical Control Strategy With Fault Ride-Through Capability for Variable Frequency Transformer

Bharath Babu Ambati, Parag Kanjiya, Vinod Khadkikar, *Member, IEEE*,
Mohamed Shawky El-Moursi, *Member, IEEE*, and James L. Kirtley Jr., *Fellow, IEEE*

Abstract—A variable frequency transformer (VFT) is being considered as a new alternative to the classical back-to-back high voltage direct current (HVDC) system for interconnection of two asynchronous networks. The VFT is a retrospective form of frequency converter using the wound rotor induction machine (WRIM), which converts the constant frequency input into a variable frequency output. The prime objective of VFT is to achieve controlled bidirectional power transfer between the two asynchronous networks. This paper presents a detailed working principle of VFT technology and proposes a new hierarchical control strategy for establishing the VFT connection with two power systems to achieve bidirectional power transfer between them. Also, to restrict the grid fault propagation from one side of the VFT to the other side, a series dynamic braking resistor based fault ride-through (FRT) scheme is proposed. The performance of the VFT during synchronization process, steady-state, dynamic, and the grid fault conditions is evaluated using the real-time hardware in-loop (HIL) system. The plant is simulated in real time using OPAL-RT real-time simulator while the control algorithm is implemented in digital signal processor to carry out HIL study. All the important results supporting the effectiveness of the proposed control strategy and FRT scheme are discussed.

Index Terms—Fault propagation, hierarchical control, power flow control, rotating transformer, series dynamic breaking resistor (SDBR), variable frequency transformer (VFT).

I. INTRODUCTION

IN GENERAL, the interconnection of two different power networks with controlled power transfer capability can be achieved by a synchronous tie using a phase-shifting transformer or by an asynchronous tie using classical back-to-back high voltage direct current (HVDC) link. In the modern power systems, establishing a synchronous tie between two power networks would be a challenging task especially when one or both the networks experience a slight variation in their frequencies [1]. Moreover, the use of phase-shifting transformers in synchronous ties suffers from the drawbacks such as slow and

step-wise controls [2]. This further causes wear and tear of tap changer contacts. Although, the use of power electronic controlled phase-shifting transformer can eliminate these drawbacks, they introduce additional problems such as harmonics, resonance, vulnerability to voltage surges, and reduced overloading capability due to their low thermal time constant [2], [3]. On the other hand, a back-to-back HVDC link can be established between any two power networks to achieve the controlled power flow between them. A line commutated converter (LCC)-based HVDC link suffers with the bottlenecks such as large reactive power requirements, lower thermal time constant, and lack of inertia for natural damping. Whereas, the voltage source converter (VSC)-based HVDC link can control the reactive power unlike LCC-based HVDC link. But, the inertia contribution and frequency response are still the challenges for HVDC technologies. Alternatively, the use of variable frequency transformer (VFT) for asynchronous interconnection can improve the system inertia and frequency control.

The VFT was first developed by General Electric Company in 2004 to achieve the interconnection of two different power networks [2]. A VFT is a controllable bidirectional power transfer device between the two asynchronous power networks that consists of wound rotor induction machine (WRIM) and a dc motor drive [2]. The presence of rotating mass (of both WRIM and dc motor) adds inertia to the power systems and thereby improves the stability during system disturbances. The VFT offers significant benefits over the widely installed LCC-HVDC link [4]–[6], mainly, lower reactive power requirements, harmonic-free power transfer, and higher system stability.

Basic concept and design aspects of 100 MW VFT is presented in [2]. The performance of VFT during steady-state, dynamic, and transient conditions is evaluated using simulation studies in [7]–[12]. In [13], the offshore wind park is connected to the grid through VFT to reduce the power fluctuations using the PID damping torque controller of the dc motor drive. Moreover, the use of brushless doubly fed induction machine (BDFIM) with squirrel cage rotor as alternative VFT configuration is reported in [6]. In which, the dual stator winding with different pole numbers with a ratio of 1:3 is used to avoid space harmonics concerns. The operating performance and maintenance of VFT is discussed in [15] and [16].

The steady-state analysis of the VFT is well established in the literature [2]–[12], but the problem of fault propagation and the fault ride-through (FRT) enhancement is not addressed so far. As

Manuscript received October 28, 2013; revised February 27, 2014 and May 19, 2014; accepted June 21, 2014. Paper no. TEC-00638-2013.

B. B. Ambati, P. Kanjiya, and V. Khadkikar are with the Center for Energy, Masdar Institute of Science and Technology, Abu Dhabi, 54224, UAE (e-mail: bambati@masdar.ac.ae; pkanjiya@masdar.ac.ae; vkhadkikar@masdar.ac.ae).

M. S. El-Moursi and J. L. Kirtley Jr. are with the Department of Electrical Engineering and Computer Science, Massachusetts Institute of Technology, Cambridge, MA 02139 USA. (e-mail: melmoursi@mit.edu; kirtley@mit.edu).

Color versions of one or more of the figures in this paper are available online at <http://ieeexplore.ieee.org>.

Digital Object Identifier 10.1109/TEC.2014.2336981

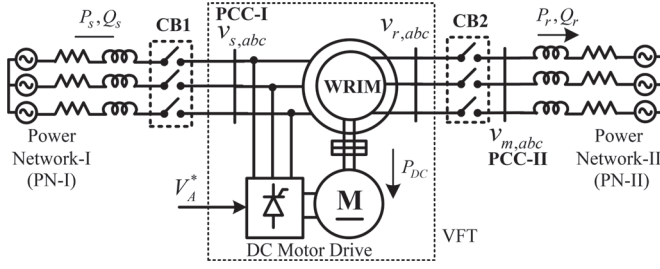


Fig. 1. VFT system configuration.

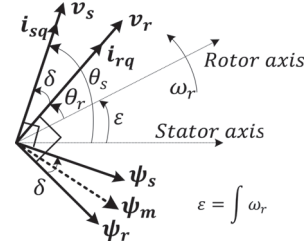


Fig. 2. Stator and rotor fluxes and voltages in VFT.

87 the fault propagation is a critical issue that affects power system
88 reliability and security, the FRT protection schemes should be
89 deployed in the VFT. In addition to that, the detailed control
90 strategy for VFT is not presented in the literature.

91 This paper presents a detailed hierarchical control strategy
92 for the VFT to achieve the following functions: establish a con-
93 nection between two power systems, power transfer control,
94 and FRT operation. Furthermore, a new topology of VFT com-
95 prising a series dynamic braking resistor (SDBR) is proposed
96 to enhance the FRT capability. A number of states are defined
97 for VFT operation to effectively connect it, operate it in steady
98 state, and protect it during the grid faults. The proposed control
99 strategy and VFT configuration are validated using real-time
100 hardware in-loop (HIL) simulation. The plant is simulated in
101 real time using OPAL-RT real-time simulator while the control
102 algorithm is implemented in dSPACE-1103 to carry out HIL
103 study.

104 II. VARIABLE FREQUENCY TRANSFORMER

105 Fig. 1 shows the VFT system configuration that consists of
106 a WRIM mechanically coupled with a dc motor drive. The
107 three-phase stator and rotor windings of WRIM are connected
108 to two asynchronous power networks namely power network-I
109 (PN-I) and power network-II (PN-II) as illustrated in Fig. 1. The
110 frequencies and/or phase angles of both PN-I (f_s and θ_s) and
111 PN-II (f_m and θ_m) could be different in actual application.

112 To connect the stationary VFT to the PN-I and PN-II sim-
113 ultaneously, the frequencies (f_s and f_m) and phase angles (θ_s and
114 θ_m) should be identical. It is difficult to achieve this condition in
115 practical system. Therefore, the following approach is deployed
116 with the VFT to make this asynchronous interconnection.

- 117 1) Connect the PN-I directly to the stator side of the VFT
118 (by closing CB1) while keeping the rotor stationary and
119 circuit breaker CB2 open.
- 120 2) Measure the frequency f_r and phase angle θ_r of the volt-
121 age induced in the rotor windings ($v_{r,abc}$) at the termi-
122 nals of CB2 (when the rotor is stationary, $f_r = f_s$ and
123 $\theta_r = \theta_s$).
- 124 3) Measure the frequency f_m and phase angle θ_m of PN-II
125 voltage ($v_{m,abc}$) available on the other side of CB2.
- 126 4) Control the rotor speed to change f_r by using the dc motor
127 drive to achieve $f_r = f_m$.
- 128 5) Adjust the rotor position (θ_r) using the dc motor drive to
129 make $\theta_r = \theta_m$.

- 6) The synchronization between voltages $v_{r,abc}$ and $v_{m,abc}$ is
130 achieved by steps 4 and 5, then the CB2 can be closed
131 to establish the interconnection between both networks
132 through VFT.
133

134 Here onwards, the points 4 and 5 are referred as frequency
135 matching and phase angle matching, respectively. A control
136 algorithm required to control the dc motor drive in VFT is
137 developed in Section V.

138 III. VFT CONCEPT AND POWER FLOW

139 Based on the existing literature, the working principle and
140 the active and reactive power flow through the VFT have not
141 been discussed in detail. In addition to that, FRT operation and
142 protection strategy have not been addressed. Hence, the detailed
143 VFT model is developed to study all the operational aspects for
144 steady-state, dynamic, and transient conditions.

145 A. Active Power Transfer and Control

146 The synchronization procedure described in the previous sec-
147 tion is used to connect both power networks in Fig. 1. Conse-
148 quently, both the stator and rotor fluxes will be in synchronism
149 irrespective of the rotor speed with a specific phase angle dif-
150 ference represented as load angle (δ). The controllability of this
151 load angle δ and its effect on active power transfer between both
152 networks is analyzed in this subsection.

153 The stator and rotor voltage vectors and the respective flux
154 vectors referred to stator are shown in Fig. 2. The instantaneous
155 stator flux (ψ_s), air-gap flux (ψ_m) and rotor flux (ψ_r) vectors
156 in the stationary reference frame can be expressed as

$$\psi_s = L_s \mathbf{i}_s + L_m (\mathbf{i}_r e^{j\epsilon}) \quad (1)$$

$$\psi_m = L_m (\mathbf{i}_s + (\mathbf{i}_r e^{j\epsilon})) \quad (2)$$

$$\psi_r = L_r \mathbf{i}_r + L_m (\mathbf{i}_s e^{-j\epsilon}) \quad (3)$$

157 where L_s , L_r , and L_m represent the equivalent stator, rotor,
158 and mutual inductances referred to stator side; \mathbf{i}_s and \mathbf{i}_r are the
159 stator and rotor currents, respectively. ϵ is the angular displace-
160 ment between the stator and rotor fluxes and ω_r is the angular
161 (mechanical) speed of the rotor.

162 From Fig. 2 and (1)–(3), the expression for the electromag-
163 netic torque (T_e) can be obtained as [14]

$$T_e = \frac{2p}{3} \frac{L_m}{L_s L_r} \text{Im} [\psi_s \psi_r^*] = \frac{2p}{3} \frac{L_m}{L_s L_r} |\psi_s| |\psi_r^*| \sin \delta. \quad (4)$$

164 The aforementioned relationship shows that the electromag-
 165 netic torque developed is a cross product of stator and rotor
 166 fluxes, i.e., the product of magnitudes of ψ_s , ψ_r , and the sine
 167 of the angle δ between both the fluxes. On the other hand, gener-
 168 al expression for the developed electromagnetic torque in any
 169 reference frame (d - q or α - β) can be written as

$$T_e = k\psi_m i_q \quad (5)$$

170 where k is the torque constant, and i_q is component of current
 171 vector in quadrature with ψ_m . Here, the quadrature component
 172 of current refers to stator/rotor current as the angle between ψ_m
 173 and ψ_s or ψ_m and ψ_r is very small.

174 From the basic integral relation between the flux and volta-
 175 ge, a current that is in quadrature with the flux is in-phase or
 176 out-of-phase with the voltage and hence responsible for active
 177 power flow. In general, the VFT is connected between the two
 178 power systems whose voltages are fairly constant and hence the
 179 magnitudes of ψ_s , ψ_r , and ψ_m can be treated as constants.
 180 Therefore, from (4) and (5) it can be deduced that the torque
 181 developed/imposed on the rotor is proportional to 'Sin δ ' and active
 182 component of stator/rotor current. If the displacement angle
 183 ε in Fig. 2 is changed by applying external torque through the
 184 dc motor drive, the angle δ and hence electromagnetic torque
 185 developed in the WRIM will change according to (4). Conse-
 186 quently, it changes the active current (i_q) as per (5). It can be
 187 observed that the active current variation is in proportion to δ
 188 (as the δ is very small, $\text{Sin } \delta \approx \delta$), which is analogous to a series
 189 inductor behavior. The generalized active power flow through
 190 the series inductor is expressed by

$$P = \frac{V_s V_r}{X_s} \sin \delta. \quad (6)$$

191 Therefore, for the case of VFT, considering a stator to rotor
 192 turns ratio of 1:1, and neglecting the losses in the system, the
 193 active power transfer (P_{VFT}) in terms of the stator and rotor
 194 voltages, from Fig. 2, can be written as

$$P_{VFT} = \frac{V_s V_r}{X_s} \sin(\theta_s - (\theta_r + \varepsilon)) \quad (7)$$

195 where V_s and θ_s are the *rms* stator voltage and its phase angle,
 196 respectively; V_r and θ_r are the *rms* rotor voltage and its phase
 197 angle, respectively; and X_s is the series equivalent inductive
 198 reactance offered by the VFT. The term ε in (7) is the time
 199 integral of ω_r to be controlled by the dc motor drive.

200 By neglecting the leakage reactance and magnetizing current
 201 (i.e., power factors close to unity) of the VFT [2], the mechanical
 202 power handled by the dc motor drive can be expressed as

$$P_{dc} = P_s - P_r = V_s I_s - V_r I_r \quad (8)$$

203 where I_s and I_r are the *rms* values of the active component of sta-
 204 tor and rotor currents, respectively. Considering volt/hertz/turn
 205 and MMF balance between the stator and rotor windings of the
 206 VFT, the above expression can be rewritten as [2]

$$P_{dc} = V_s I_s - \left(\frac{V_s}{N_s f_s} N_r f_r \right) \left(\frac{I_s N_s}{N_r} \right) = V_s I_s \left(1 - \frac{f_r}{f_s} \right) \quad (9)$$

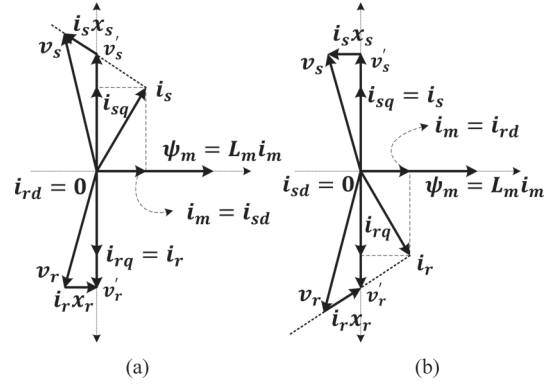


Fig. 3. Reactive power flow concept in the VFT. (a) $v_s > v_r$ (b) $v_s < v_r$

where N_s and N_r are the number of turns in the stator and 207
 208 rotor windings of VFT, respectively. From (9), it is clear that the
 209 power absorbed by the dc motor drive is a function of frequency
 210 difference between both the power networks and the power
 211 being transferred through the VFT. Also, from (9), the torque
 212 expression for the dc motor can be written as

$$T_{dc} = \frac{P_{dc}}{\omega_r} = \frac{V_s I_s \left(1 - \frac{f_r}{f_s} \right)}{2\pi \frac{120(f_s - f_r)/p}{60}} = \frac{p V_s I_s}{2 \cdot 2\pi f_s} \quad (10)$$

213 where p is number of poles in the WRIM. From (10), it can 213
 214 be noticed that the torque developed by the dc motor drive is
 215 independent of speed of rotation. Assuming the constant stator
 216 voltage in (10), it can be noticed that by changing the torque
 217 applied through dc motor drive, the stator active current (I_s)
 218 can be changed. This proves the correlation between torque
 219 applied by dc motor drive and active current transferred through
 220 VFT according to (5). A simple armature voltage controlled
 221 four quadrant dc drive can be employed to regulate the torque
 222 produced by the dc motor and thereby active power transfer.

B. Reactive Power Transfer 223

224 Stator and rotor reactive currents (i_{sd} and i_{rd}) of VFT may
 225 consist of two components: 1) the magnetizing current required
 226 for VFT operation (i_m); and 2) the reactive current transferred
 227 between the two networks. The amount of reactive current suppl-
 228 ied/absorbed by each network is dependent on the voltage mag-
 229 nitudes at the stator (PCC-I) and rotor (PCC-II) terminals.
 230 Regardless of slight difference in grid voltages on both sides,
 231 the VFT maintains the volt/hertz/turn balance between induced
 232 stator (v'_s) and rotor (v'_r) voltages by circulating the appropriate
 233 amount of reactive current between both the networks.

234 Two different cases are demonstrated to show the reactive
 235 power flow dependency on the voltage magnitudes on both sides
 236 of VFT as illustrated in Fig. 3. The stator and rotor resistances
 237 are neglected and it is assumed that the active current transferred
 238 between the stator and rotor is constant ($i_{sq} = -i_{rq}$) throu-
 239 ghout the operation. Fig. 3(a) represents the case where the stator
 240 voltage is slightly higher than the rotor voltage referred to stator
 241 side (i.e., $v_s > v_r$). Assuming the induced stator voltage (v'_s)

is constant, any increase in v_s causes increase in i_s according to $v_s = v'_s + i_s x_s$. For the fixed active power transfer, active current (i_{sq}) is constant and hence reactive current (i_{sd}) has to increase in order to accommodate the change in i_s . In Fig. 3(a), the stator voltage magnitude is considered such that whole magnetizing current (i_m) required for VFT operation comes from the stator (i.e., $i_m = i_{sd}$ and $i_{rd} = 0$). Thus, further increase in the stator voltage magnitude leads to i_{sd} higher than i_m , that makes $i_{rd} = -(i_{sd} - i_m)$ which is the net reactive current transferred from PN-I to PN-II through VFT. Accordingly, any reduction in stator voltage magnitude drives the stator and rotor sides to supply the required magnetizing current i_m for VFT operation.

The vector diagram corresponding to the case where full magnetizing current is drawn from the rotor side due to higher rotor voltage is shown in Fig. 3(b). Similar to the aforementioned case, any further increase in the rotor voltage in Fig. 3(b) leads to reactive power flow from PN-II to PN-I.

It is obvious that the reactive power flow into/through VFT is uncontrolled and is mostly dependent on the terminal voltage magnitudes of v_s and v_r . The VFT requires a fixed amount of reactive power to meet the constant magnetization demand regardless of the amount and/or direction of active power transfer. The stator and rotor currents through VFT can be obtained from the steady-state equivalent circuit for particular voltage conditions and reactive powers can be computed as

$$Q_s = |\nu_s| |i_{sd}| = \text{Im} [\nu_s i_s^*] \quad (11)$$

$$Q_r = |\nu_r| |i_{rd}| = \text{Im} [\nu_r i_r^*]. \quad (12)$$

For the power flow directions shown in Fig. 1, the reactive power absorbed by VFT (Q_m) at any operating condition is the difference between stator and rotor reactive powers, i.e.,

$$Q_m = Q_s - Q_r. \quad (13)$$

IV. SDBR PROTECTION SCHEME FOR VFT

As discussed in the previous section, during the steady-state operation, VFT is analogous to a series inductor. Therefore, during a voltage dip resulted from the grid fault in one of the power networks, the other network is forced to supply a large fault currents. This indicates the propagation of a fault from the faulted network to the healthy power network through VFT. This fault propagation phenomenon associated with VFT has not been discussed in the literature. To demonstrate the problems associated with the fault propagation, a fault condition is considered at PN-II as shown in Fig. 1. This grid fault (or voltage dip) has the following consequences unless appropriate protective measures are taken:

- 1) large fault currents from the stator side;
- 2) temporary disconnection of VFT due to CB1 opening;
- 3) oscillations/instability in PN-I due to system dynamics;
- 4) slow post fault recovery due to VFT disconnection;
- 5) possible requirement of VFT resynchronization;
- 6) damage to VFT windings in the event of protection failure.

This paper introduces an appropriate FRT scheme within the VFT system using SDBR to overcome the issue of fault propagation as shown in Fig. 4. The SDBR protection scheme is

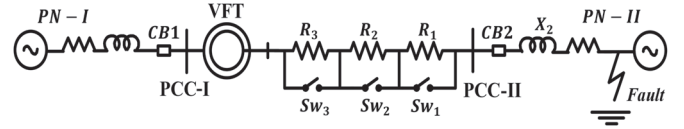


Fig. 4. Single line diagram of SDBR protection scheme for VFT.

identified as simple and economic solution for enhancing the FRT capability and transient performance of VFT in response to symmetrical and asymmetrical grid faults. It can be noted that, four different combinations of power flow direction (PN-I to PN-II or PN-II to PN-I) and the grid fault (in PN-I or PN-II) are possible in the VFT. The SDBR scheme that can prevent the fault propagation in all four possible cases can be designed using a simple approach by considering a power flow from PN-I to PN-II and the grid fault in PN-II as described in the following.

A. Series Resistance Selection

According to the design criteria, the SDBR should limit the fault current by acting as a voltage booster against the voltage in PN-II at the rotor terminals and protect the healthy network (PN-I) connected to the stator terminal. To be able to work with various levels of grid faults (based on magnitudes of voltage dip), the SDBR should have different combination of resistors. The SDBR with n resistors can realize $(2^n - 1)$ combinations of resistances. The maximum and minimum possible resistance values of SDBR should be selected based on the following two scenarios.

1) *Voltage Dip Operation:* During the most severe grid fault, the voltage appears on the rotor terminals should be higher than the minimum allowable rotor voltage (V_{r_min}). The maximum value of series resistance ($R_{SDBR_max} = R_1 + R_2 + \dots + R_n$) required to achieve this during the worst case voltage dip can be calculated using the following:

$$V_{\text{fault_min}} + \frac{P_{\text{rated}}}{3V_{r_min}} R_{\text{SDBR_max}} \geq kV_{r_min} \quad (14)$$

where $V_{\text{fault_min}}$ is the lowest possible grid voltage (at PCC-II) during the grid fault on PN-II, P_{rated} is the rated power transfer capability of VFT, and k is safety margin (>1) to take care of the lagging power factor.

2) *Overvoltage Protection:* The designed SDBR should not cause the overvoltage across the rotor terminals in any case such as small voltage dips. The minimum value of series resistance (R_{SDBR_min}) that prevents the rotor overvoltage can be computed from the following equation:

$$V_{\text{fault_max}} + \frac{P_{\text{rated}}}{3V_{r_rated}} R_{\text{SDBR_min}} \leq 3V_{r_rated} \quad (15)$$

where $V_{\text{fault_max}}$ is the grid voltage (at PCC-II) during the minor voltage dip that can trigger the SDBR. For the present case of SDBR with three resistances, the value of different resistors can be calculated from the maximum and minimum values of

331 SDBR resistances obtained through (14) and (15) as follows:

$$\begin{aligned}
 R_1 &= R_{\text{SDBR_min}} \\
 R_2 &= \frac{1}{3} [R_{\text{SDBR_max}} - R_{\text{SDBR_min}}] \\
 R_3 &= \frac{2}{3} [R_{\text{SDBR_max}} - R_{\text{SDBR_min}}].
 \end{aligned} \quad (16)$$

332 B. Static AC Switch Selection

333 Three SDBR resistors can be inserted into the circuit by controlling the static ac switches Sw_1 , Sw_2 , and Sw_3 , respectively. Three ac switches are required for switching the resistors (R_1 , R_2 , and R_3) in each phase as per Fig. 4. Therefore, a total of nine resistors (R_1 , R_2 , and R_3 for each phase) and nine ac switches are deployed to realize the SDBR protection scheme.

339 The current rating of ac switches in SDBR scheme should be equal to the rated VFT current as they remain closed during the steady-state operation. And, the voltage rating of the switches should be equal to the product of rated VFT current and corresponding resistor value. It is worthy to note that the switching losses are absent (as switches are always closed) during the steady-state operation and therefore, the switches with low conduction losses are preferred for this SDBR scheme.

347 The ac switches can be realized using either antiparallel thyristors (low cost) or antiseres IGBTs (high cost). The choice of the switch depends on the speed requirement of resistor insertion during the fault. The antiparallel thyristor switch has a maximum of half cycle delay in operation as it breaks the current at next zero crossing while, antiseres IGBT switch can break the current instantaneously.

354 The WRIM in the VFT system possesses large thermal time constant and can easily handle the current surge resulted from the delay in ac switch opening. Therefore, the low cost antiparallel thyristor switches are used as ac switches in SDBR protection scheme.

359 V. PROPOSED HIERARCHICAL CONTROL STRATEGY

360 This section describes the overall control of VFT and SDBR. The dc motor drive is the only controllable device in a VFT system that can regulate the power flow between two power networks. However, as highlighted in the previous section SDBR is an additional controllable device for the restriction of fault propagation. A comprehensive hierarchical strategy, with all the necessary controls, is proposed in three operational stages.

367 When the stator is directly connected to PN-I and circuit breaker CB2 is open, the dc motor drive is to be controlled to achieve the frequency matching ($f_r = f_m$) and phase angle matching ($\theta_r = \theta_m$). This part of control is realized in first two stages (Stage-I and Stage-II) of the proposed hierarchical control. Once the connection is established between both the power networks through VFT, the power transfer control is carried out in Stage-III.

375 The control block diagram depicting these three stages of the proposed hierarchical control is shown in Fig. 5. A four-quadrant armature voltage control method is employed for dc drive in the proposed hierarchical control. The changeover from

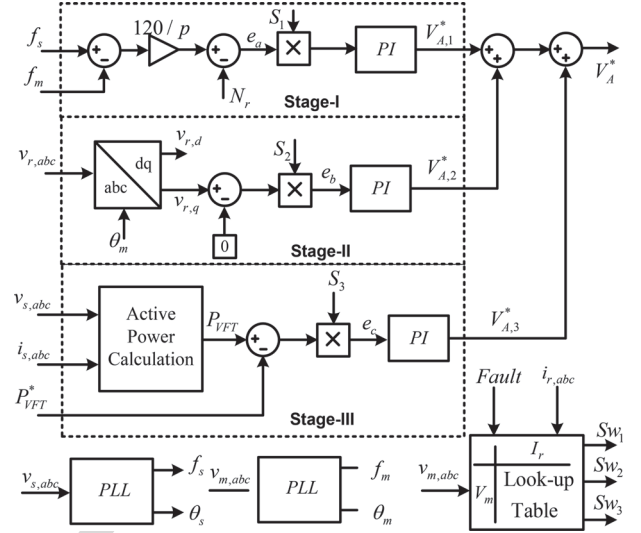


Fig. 5. Proposed hierarchical control strategy for synchronization and power transfer control in VFT.

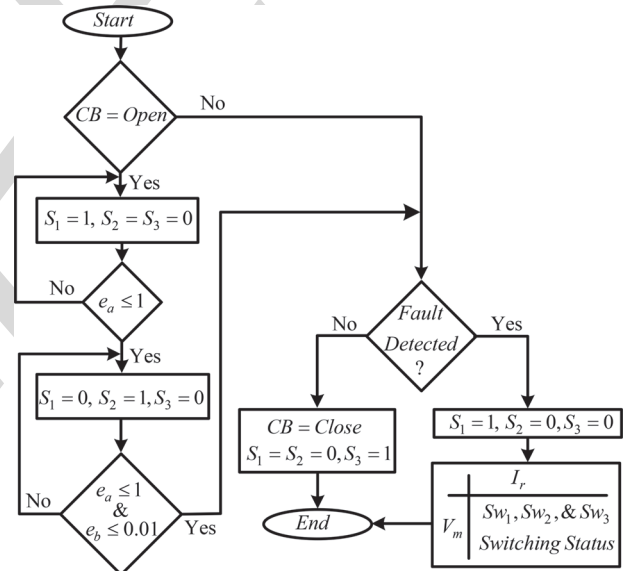


Fig. 6. Flow chart for hierarchical control strategy and SDBR control.

379 one stage to another is realized using the states S_1 , S_2 , and S_3 as illustrated in Fig. 5 with the predefined hierarchy depicted in Fig. 6. The control of SDBR protection scheme is also incorporated in the flow chart of Fig. 6. The objective and control of VFT in each stage of hierarchical control is discussed in the following subsections.

A. Stage-I: Frequency Matching

385 Initially when the stator of WRIM is connected to PN-I, the rotor is stationary and CB2 is open, the command $S_1 = 1$ is issued to start the frequency matching stage. At this condition the frequency of rotor voltage f_r has to be changed from $f_r = f_s$ to $f_r = f_m$. To achieve this desired frequency change, the equivalent rotor speed at which the rotor of VFT should be

392 driven by dc motor drive is

$$N_r^* = \frac{120(f_s - f_m)}{p}. \quad (17)$$

393 The reference (N_r^*) and actual (N_r) speeds are compared,
394 and the error, e_a , is processed through the PI controller to gen-
395 erate the necessary armature voltage ($V_{A,1}^*$) for the armature
396 controlled dc motor drive (shown in Stage-I of Fig. 5). Once,
397 the mean of absolute speed error (e_a) goes below 1 r/min, S_1
398 becomes low and S_2 becomes high as shown in the flow chart
399 given in Fig. 6. Thereafter, high state of S_2 enables the next
400 stage of hierarchical control.

401 B. Stage-II: Phase Angle Matching

402 Subsequent to the frequency matching, the next objective is
403 to achieve the phase angle matching between $v_{r,abc}$ and $v_{m,abc}$
404 (i.e., $\theta_r = \theta_m$). Applying $abc-dq$ transformation on the mea-
405 sured rotor voltages ($v_{r,abc}$) using the phase angle (θ_m) of PN-II
406 voltage ($v_{m,abc}$), obtained from the phase locked loop (PLL),
407 gives the direct ($v_{r,d}$) and quadrature ($v_{r,q}$) components of rotor
408 voltages referred to PN-II voltage phasor. When the rotor volt-
409 age phase angle (θ_r) is exactly equal to θ_m , the computed $v_{r,q}$
410 becomes zero. In other words, by making $v_{r,q} = 0$, the phase
411 angles can be matched (θ_r and θ_m). To achieve this, a PI con-
412 troller is used over the $v_{r,q}$ for generating the necessary armature
413 voltage ($V_{A,2}^*$) to change the rotor position (shown in Stage-II
414 of Fig. 5). As soon as the mean of the absolute phase angle error
415 (e_b or $v_{r,q}$) goes below certain margin (say 1%), S_2 goes low
416 indicating the completion of Stage-II (shown in Fig. 6).

417 After frequency and phase angle matching are completed,
418 the CB2 closes to establish the connection between both the
419 networks through VFT. Subsequently, S_3 goes high to enable
420 the power transfer controller.

421 C. Stage-III: Power Transfer Control

422 Actual power transfer (P_{VFT}) from PN-I to PN-II is measured
423 on the stator side of VFT and compared with the reference
424 power (P_{VFT}^*). The error is passed through the PI controller
425 to generate the necessary armature voltage ($V_{A,3}^*$) and thus to
426 control the torque developed by the dc motor drive (T_{dc}). The
427 torque produced by dc motor drive dynamically adjusts the angle
428 ε to achieve the desired load angle δ that makes $P_{VFT}^* = P_{VFT}$
429 as per (7).

430 The reference armature voltage (V_A^*) for the dc motor drive
431 is expressed as follows:

$$V_A^* = V_{A,1}^* + V_{A,2}^* + V_{A,3}^*. \quad (18)$$

432 During the power transfer control, any change in the networks
433 frequencies forces the rotor to adjust its speed according to (17).

434 D. SDBR-Based Fault Ride-Through Control

435 The SDBR control and fault detection is integrated in the hier-
436 archical control strategy as shown in Fig. 6. When the grid fault
437 occurs, the power transfer control should saturate at its prefault
438 value to avoid rotor acceleration in response to fault conditions.
439 This is achieved by forcing $S_3 = 0$ to keep the corresponding

PI controller output at its prefault value. Whereas, the command
 $S_1 = 1$ (frequency matching loop) is reissued during the fault
to damp out the rotor oscillations by controlling the torque of
the dc motor drive. Simultaneously, there is a need to insert a
suitable combination of resistors in SDBR that prevent the fault
propagation from the faulted network to the healthy network.
This is obtained using a two-dimensional (2 D) lookup table
based on VFT current and fault voltage magnitudes. The out-
put of lookup table is status of switches S_{w1} , S_{w2} , and S_{w3}
that inserts an appropriate combination of R_1 , R_2 , and R_3 . The
switches S_{w1} , S_{w2} , and S_{w3} of each phase are simultaneously
controlled for balanced faults while they are controlled inde-
pendently for each phase during the unbalance faults. After the
fault is cleared, the power transfer controller is reactivated to
maintain the power transfer control by giving the control sig-
nals $S_1 = S_2 = 0$, $S_3 = 1$. The coordination between the three
stages of the proposed hierarchical control and the proposed
SDBR control is shown in Fig. 6.

458 VI. REAL-TIME HARDWARE IN-LOOP VALIDATION

459 The proposed hierarchical control strategy and SDBR scheme
460 for VFT are verified using a real-time HIL implementation. The
461 control algorithm is implemented in the digital signal processor
(DSP) board, DS1103 from dSPACE at a step size of 50 μ s. The
462 plant (VFT test system and SDBR scheme) is emulated using
463 the OPAL-RT real-time simulator. The communication between
464 the controller and the plant is carried out through ADC and DAC
465 ports of DS1103 and OPAL-RT.

466 Due to high torque requirement by the VFT system during
467 low speed operations, a geared dc motor with a mechanical gear
468 of ratio 1:10 is used instead of conventional dc motor. The use
469 of geared dc motors can significantly reduce the size of the
470 dc motor during the actual applications of VFT. The system
471 specifications and the machine parameters of VFT test system
472 are given in Table I.

474 A. Steady-State Performance

475 The performance of VFT system during the three stages of
476 proposed hierarchical control is shown in Figs. 7–9. All the re-
477 sults are given in per unit values with 1 div = 1 p.u. The dc
478 motor drive power P_{dc} and speed N_r are represented on the
479 basis of 100 W and 60 r/min for a better visualization of their
480 dynamics. The PN-I operates at 400 V/50 Hz while the PN-II
481 operates at 392 V/49 Hz. The effectiveness of each stage of hier-
482 archical control and the transition from one stage to another can
483 be seen from Fig. 7. When VFT is stationary the frequency f_r
484 of the induced rotor voltage ($v_{r,a}$) is 50 Hz while the frequency
485 f_m of PN-II voltage ($v_{m,a}$) is 49 Hz. As highlighted in Section
486 II, to close the circuit breaker CB2, synchronization should be
487 established between the $v_{r,a}$ and $v_{m,a}$. Therefore in Stage-I,
488 with the frequency matching command $S_1 = 1$, the rotor speed
489 N_r is controlled to change f_r such that $f_r = f_m$. By the end
490 of Stage-I (just before t_1), the frequency of $v_{r,a}$ is achieved
491 equal to 49 Hz by regulating the VFT rotor speed at 0.5 p.u.
492 (30 r/min) as per (17). Subsequent to successful completion of
493 Stage-I at t_1 , the status of commands S_1 and S_2 automatically

TABLE I
 SYSTEM SPECIFICATIONS

WRIM specifications and parameters	
Power network-I	400 V, 50 Hz
Power network-I series inductance	0.03 p.u.
Power network-II	392 V, 49 Hz
Power network-II series inductance	0.052 p.u.
WRIM specifications and parameters	
Rated apparent power	4150 VA
Rated active power	3500 W
Rated voltage and frequency	400 V, 50 Hz
Number of poles	4
Stator to rotor turns ratio	400/400
Stator resistance	0.01965 p.u.
Stator inductance	0.0397 p.u.
Rotor resistance referred to stator	0.01965 p.u.
Rotor inductance referred to stator	0.0397 p.u.
Magnetizing (mutual) inductance	1.354 p.u.
Inertia constant	0.09526 s
DC motor drive specifications	
Rated output power	500 W
Rated armature voltage	500 V
Rated field voltage	300 V
Number of poles	4
Mechanical gear ratio	1/10
Electrical connection of dc drive	To power network-I

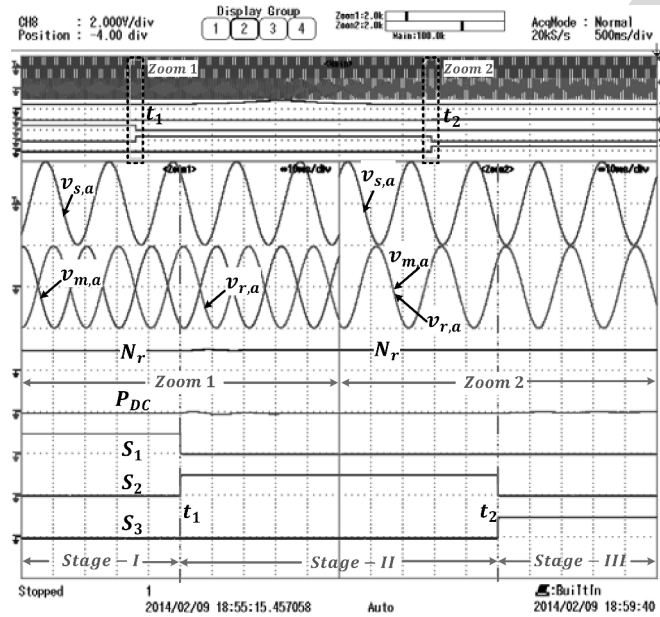


Fig. 7. Different stages in the proposed hierarchical control.

494 changes to $S_1 = 0$ and $S_2 = 1$ (Zoom1). In Stage-II, the phase
 495 angle matching of $v_{r,a}$ and $v_{m,a}$ is performed. To match the
 496 phase angles of both the voltages by changing the instantaneous
 497 rotor position of VFT, the speed of dc motor drive temporarily
 498 deviates from its reference speed. This operation can be seen
 499 from the temporary variations in N_r and the power handled by
 500 the dc drive (P_{dc}). The successful matching of frequencies and
 501 phase angles of $v_{r,a}$ and $v_{m,a}$ can be observed from Zoom2
 502 (just before time t_2). Stage-II ends at t_2 where the status of
 503 commands S_2 and S_3 are changed to $S_2 = 0$ and $S_1 = 1$ and

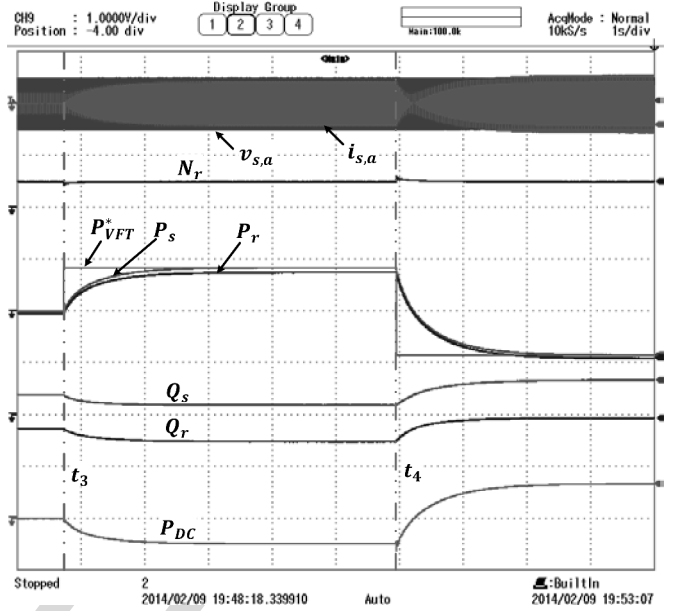


Fig. 8. Power control using the hierarchical control (dynamic performance).

the circuit breaker CB2 is closed to initiate the power transfer
 stage (Stage-III).

The performance of VFT during Stage-III is depicted in
 Figs. 8 and 9. According to power flow directions considered in
 Fig. 1, the positive value of P_{VFT}^* represents the power trans-
 ferred from PN-I (stator side) to PN-II (rotor side) and negative
 quantity represents the reverse power flow.

The dynamic response of VFT during sudden changes in
 power transfer command (P_{VFT}^*) is shown in Fig. 8. Initially,
 P_{VFT}^* is set equal to zero, and at t_3 , it is changed from 0 to
 0.85 p.u. It can be noticed that P_s and P_r reach the steady state
 ($P_s = P_{VFT}^*$) within 3 s. Further to check the response of VFT
 during power reversal, P_{VFT}^* is changed from 0.85 to -0.85
 p.u. at t_4 . It can be observed that VFT reaches the new steady
 state within 3 s in this case as well. Note that, due to the active
 power loss in VFT there is a small difference between P_s and
 P_r during the steady state. The active power supplied/absorbed
 by the dc drive is governed by the direction of power transfer
 and it is observed around 0.5–0.7 p.u. (around 0.012–0.015 p.u.
 on VFT power base).

The expanded view of steady-state results for P_{VFT}^* equal to
 0.85 and -0.85 p.u. is shown in Fig. 9 in Zoom1 and Zoom2,
 respectively. In Zoom1, it can be noticed that the stator current
 $i_{s,a}$ is nearly in-phase with stator voltage $v_{s,a}$ as the power
 is being transferred from PN-I to PN-II. Whereas in case of
 reverse power flow (Zoom2), $i_{s,a}$ is noticed to be almost out-of-
 phase with $v_{s,a}$. The change in Q_s and Q_r with the change in
 P_{VFT}^* (in Figs. 8 and 9) represents their uncontrolled nature as
 discussed in Section III-B. Due to this, the stator current ($i_{s,a}$)
 magnitudes are different for the same amount of active power
 flow in both directions. Note that the difference between Q_s
 and Q_r is almost constant as per (13) and is equal to the reactive
 power absorbed/required by VFT (Q_m).

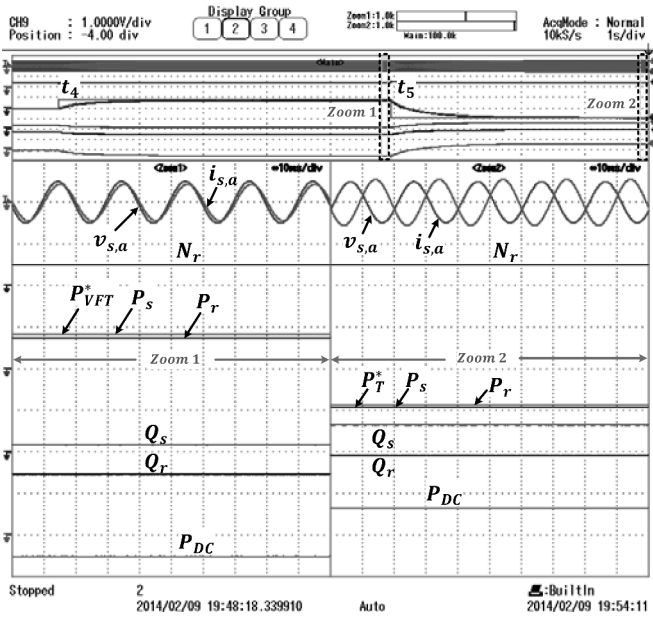


Fig. 9. Power control using the hierarchical control (steady-state performance).

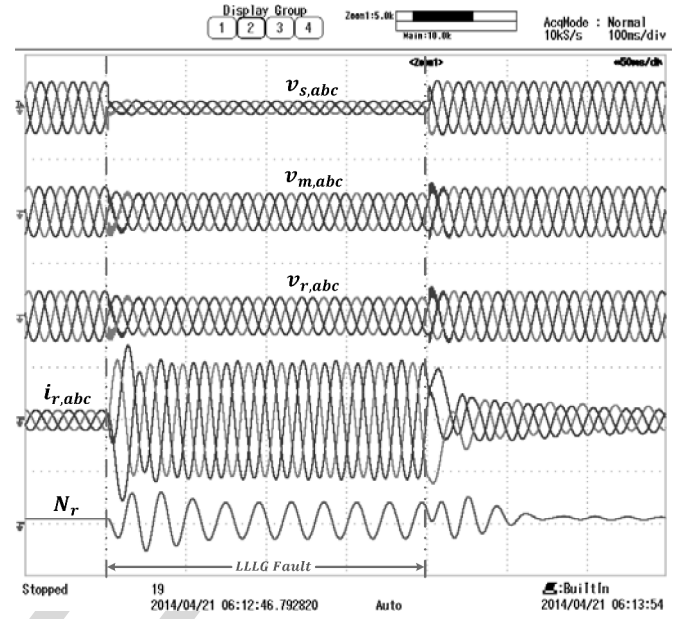


Fig. 11. VFT performance during three-phase fault in PN-I (stator side) without SDBR protection scheme.

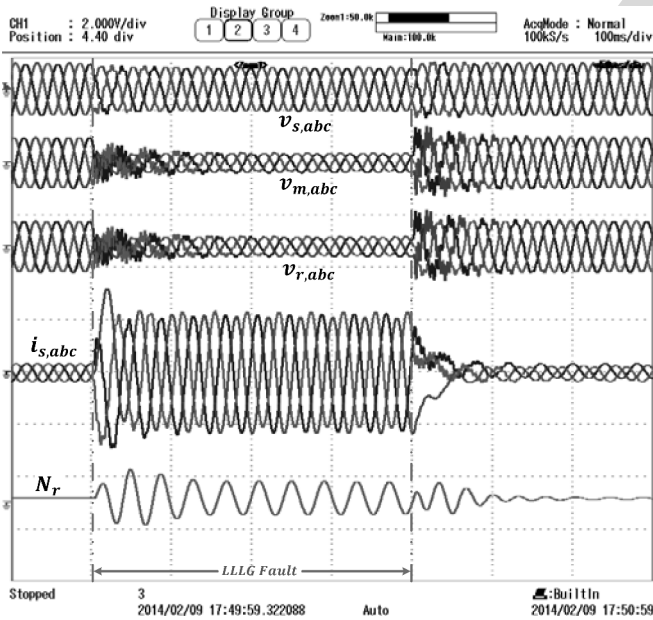


Fig. 10. VFT performance during three-phase fault in PN-II (rotor side) without SDBR protection scheme.

537 B. Fault Ride-Through Performance

538 The behavior of VFT without any additional FRT mechanism,
 539 during the three-phase grid fault at PN-II is shown in Fig. 10.
 540 The important variables that depict the fault propagation problem
 541 with VFT are shown in Fig. 10. These variables include:
 542 PN-I voltage at PCC-I ($v_{s,abc}$: 1 div = 2 p.u.), the
 543 PN-II voltage at PCC-II ($v_{m,abc}$: 1 div = 2 p.u.), the rotor
 544 voltage ($v_{r,abc}$: 1 div = 2 p.u.), current drawn from PN-I
 545 ($i_{s,abc}$: 1 div = 5 p.u.), and the rotor speed (N_r : 1 div = 5

p.u.). Prior to the grid fault, the system is under steady state
 546 with a power transfer of 0.85 p.u. from PN-I to PN-II. A
 547 significant voltage dip in both PCC-II ($v_{m,abc}$) and rotor ($v_{r,abc}$)
 548 voltages and sudden rise in stator current ($i_{s,abc}$) can be noticed
 549 during the grid fault condition. The rise in stator current signi-
 550 fies that the fault in the rotor side (PN-II) is propagated to the
 551 stator side (PN-I). The fault current in PN-I reaches 5 p.u. which
 552 may cause threat to PN-I security and reliability. Moreover, the
 553 large oscillations introduced in the rotor speed (N_r) during the
 554 grid fault causes the sustained mechanical vibrations that may
 555 destroy the WRIM and dc motor bearings.
 556

The fault propagation from the stator side to rotor side during
 557 a grid fault on stator side (PN-I) is depicted in Fig. 11. It can
 558 be noticed that the rotor current rises 5 p.u. during the fault without
 559 SDBR protection. This signifies the fault propagation from PN-I
 560 to PN-II.
 561

To avoid such high fault currents and mechanical stress due to
 562 fault propagation, the SDBR protection scheme shown in Fig. 4
 563 is designed (explained in Section III). The set of specifications
 564 considered during the SDBR design are: $V_{\text{fault_min}} = 0.1$ pu,
 565 $V_{\text{fault_max}} = 0.9$ pu, $P_{\text{rated}} = 0.85$ p.u., $k = 1.1$ and $V_{r_min} =$
 566 0.9 pu. The values for $R_{\text{SDBR_max}}$ and $R_{\text{SDBR_min}}$ calculated
 567 using (14) and (15) are 4Ω and 40Ω , respectively. From (16), the
 568 SDBR resistance values computed are $R_1 = 4 \Omega$, $R_2 = 12 \Omega$,
 569 and $R_3 = 24 \Omega$ respectively.
 570

The performance of VFT with the proposed SDBR scheme
 571 during three-phase to ground fault on PN-II is shown in Fig. 12.
 572 Due to the activation of SDBR scheme during the three-phase
 573 fault, the rotor voltage ($v_{r,abc}$) is restored to the nominal level
 574 and the stator current ($i_{s,abc}$) is restricted to the maximum rated
 575 current. As the activation of SDBR does not allow the stator
 576 current to reach high value, it prevents the fault propagation
 577 through VFT. The oscillations in the speed are also reduced with
 578

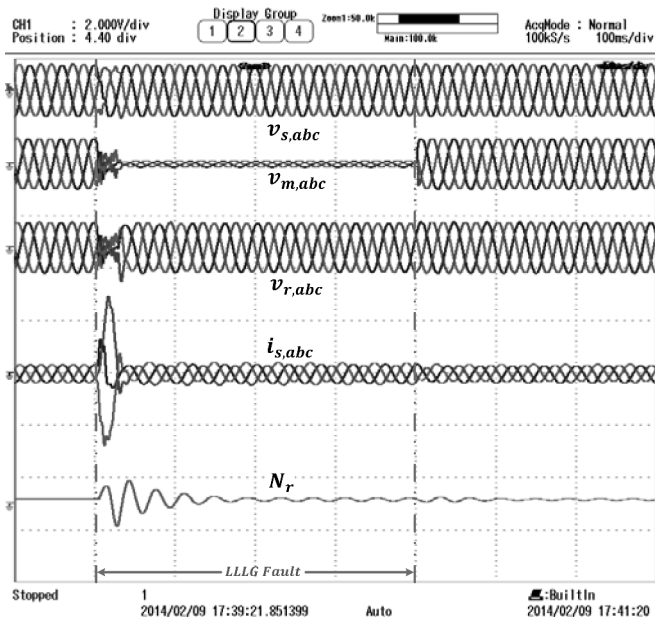


Fig. 12. VFT performance during three-phase fault in PN-II (rotor side) with the SDBR protection scheme.

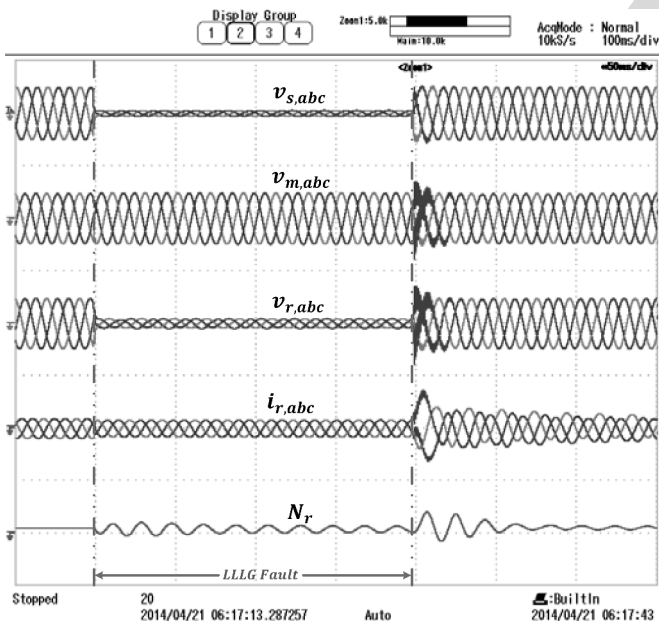


Fig. 13. VFT performance during three-phase fault in PN-I (stator side) with the SDBR protection scheme.

579 the SDBR and are damped out due to the presence of mechanical
580 inertia and opposing torque produced by the dc motor drive.

581 The performance of VFT with the proposed SDBR protec-
582 tion scheme during the three-phase to ground fault on the stator
583 side (PN-I) is depicted in Fig. 13. It can be observed that the
584 grid fault on the stator side causes a sudden dip in stator vol-
585 age, $v_{s,abc}$. During this condition, the insertion of SDBR series
586 resistance on the rotor side brings down the $v_{r,abc}$ without
587 affecting $v_{m,abc}$. This restricts the flow of fault current through

VFT to a nominal level as noticed from $i_{r,abc}$. Note that the rise
588 in $i_{r,abc}$ immediately after the fault clearance is mainly due to
589 the sudden change in stator flux caused by the abrupt recovery
590 of stator voltage.
591

The satisfactory performance during the steady-state, dy-
592 namic, and grid fault conditions proves that VFT with proposed
593 SDBR scheme and hierarchical control strategy is a potential
594 contender for the application of controlled power transfer be-
595 tween two asynchronous power networks.
596

VII. CONCLUSION

This paper presents a new hierarchical control strategy to
597 control the VFT during normal and FRT operating conditions.
598 This paper further investigates the possible fault propagation
599 issue through VFT from one network to another. The SDBR-
600 based FRT scheme has been proposed for VFT to mitigate the
601 fault propagation. The detailed working principles of the VFT,
602 all the stages of hierarchical control and FRT operation are
603 verified using the real-time HIL system.
604

The detailed results under three stages of the proposed hier-
605 archical control (frequency matching, phase angle matching, and
606 power transfer control) during steady-state and dynamic condi-
607 tions prove its comprehensiveness. The satisfactory results in
608 limiting the fault propagation through VFT during the grid faults
609 validate the effectiveness of SDBR protection scheme. In sum-
610 mary, along with the power transfer control function of VFT,
611 added capability to limit the fault propagation and inherent nat-
612 ural damping capability will make VFT an ideal solution for the
613 interconnection of micro grids in the future power systems.
614
615

REFERENCES

[1] M. P. Bahrman, "Overview of HVDC transmission," in *Proc. Power Syst. Conf. Expo.*, 2006, pp. 18–23. 617
 [2] A. Merkhof, P. Doyon, and S. Uphadayay, "Variable frequency 618
 transformer—Concept and electromagnetic design evaluation," *IEEE 619
 Trans. Energy Convers.*, vol. 23, no. 4, pp. 989–996, Dec. 2008. 621
 [3] E. Larsen, "A classical approach to constructing a power flow controller," 622
 in *Proc. IEEE Power Eng. Soc. Summer Meeting*, 1999, vol. 2, pp. 1192– 623
 1195. 624
 [4] R. J. Piwko, E. V. Larsen, and C. A. Wegner, "Variable frequency 625
 transformer—a new alternative for asynchronous power transfer" in *Proc. 626
 IEEE Power Eng. Soc. Conf. Expo.*, Durban, Jul. 2005, pp. 393–398. 627
 [5] B. Bagen, D. Jacobson, G. Lane, and H. M. Turanli, "Evaluation of the 628
 performance of back-to-back HVDC converter and variable frequency 629
 transformer for power flow control in a weak interconnection," presented 630
 at IEEE Power Eng. Soc. Gen. Meeting, Tampa, FL, USA, Jun. 24–28, 631
 2007, pp. 1–6. 632
 [6] A. S. Abdel-Khalik, A. Elserougi, S. Ahmed, and A. Massoud, "Brushless 633
 doubly fed induction machine as a variable frequency transformer," in 634
Proc. 6th IET Int. Conf. Power Electron., Mach. Drives, Mar. 2012. 635
 [7] A. H. El Din, M. A. Abdullah, and M. Ibrahim, "A Matlab/Simulink model 636
 to study the performance of the VFT for the interconnection of weak and 637
 strong AC grids," in *Proc. IEEE Int. Elect. Mach. Drives Conf.*, May 2011, 638
 pp. 1635–1640. 639
 [8] E. T. Raslan, A. S. Abdel-Khalik, M. Abdulla, and M. Z. Mustafa, "Perfor- 640
 mance of VFT when connecting two power grids operating under different 641
 frequencies," in *Proc. 5th IET Int. Conf. Power Electron., Mach. Drives*, 642
 19–21, Apr. 2010, pp. 1–6. 643
 [9] G. Chen and X. Zhou, "Digital simulation of variable frequency transfor- 644
 mers for asynchronous interconnection in power system," in *Proc. IEEE 645
 Power Eng. Soc. Transmiss. Distrib. Conf.*, 2005, pp. 1–6. 646

- 647 [10] L. Contreras-Aguilar and N. Garcia, "Accelerated time domain solution of VFT using the Poincaré map method with an embedded implicit integration algorithm" in *Proc. North Am. Power Symp.*, Calgary, Canada Sep. 2008, pp. 1–8.
- 648
- 649
- 650
- 651 [11] L. Contreras-Aguilar and N. Garcia, "Fast convergence to the steady state operating point of a VFT park using the limit cycle method and a reduced order model," in *Proc. IEEE Power Eng. Soc. Gen. Meeting*, Calgary, Canada, Jul. 2009, pp. 1–5.
- 652
- 653
- 654
- 655 [12] L. Contreras-Aguilar and N. Garcia, "Steady-state solution of a VFT park using the Newton method and a reduced order model," in *Proc. IEEE Power Tech.*, Bucharest, Rumania, Jun./Jul. 2009, pp. 1–6.
- 656
- 657
- 658 [13] L. Wang and L. Y. Chen, "Reduction of power fluctuations of a large scale grid-connected offshore wind farm using a variable frequency transformer," *IEEE Trans. Sustain. Energy*, vol. 2, no. 3, pp. 226–234, Jul. 2011.
- 659
- 660
- 661
- 662 [14] G. Poddar and V. T. Ranganathan, "Direct torque and frequency control of double-inverter-fed slip-ring induction motor drive," *IEEE Trans. Ind. Electron.*, vol. 51, no. 6, pp. 1329–1337, Dec. 2004.
- 663
- 664
- 665 [15] P. Marken, J. Roedel, D. Nadeau, D. Wallace, and H. Mongeau, "VFT maintenance and operating performance," in *Proc. Power Eng. Soc. Gen. Meeting Convers. Del. Elect. Energy*, Jul. 2008, pp. 1–5.
- 666
- 667
- 668 [16] D. Nadeau, "A 100-MW variable frequency transformer (VFT) on the Hydro-Quebec TransEnergie Network—the behavior during disturbance" in *Proc. Power Eng. Soc. Gen. Meeting*, Jun. 2007, pp. 1–5.
- 669
- 670



Bharath Babu Ambati received the B.E. degree in electrical and electronics engineering from the Sir C. R. Reddy College of Engineering (affiliated with Andhra University), Eluru, AP, India, in 2009; the M.Tech. degree in power electronics, electrical machines, and drives (PEEMD) from the Indian Institute of Technology (IIT) Delhi, New Delhi, India, in 2011; and is currently pursuing the Ph.D. degree in interdisciplinary engineering with the Masdar Institute of Science and Technology, Abu Dhabi, UAE.

From 2011 to 2012, he was with Schneider Electric India Private Limited as a Product Expert of Motion and Drives. His current research interests include power electronics, electrical machines, renewable energy generation, and power quality.



Parag Kanjiya received the B.Eng. degree in electrical engineering from the B.V.M. Engineering College, Sardar Patel University, V.V. Nagar, India, in 2009, and the M.Tech. degree in power systems from the Indian Institute of Technology Delhi (IITD), New Delhi, India, in 2011.

Since October 2011, he has been a Research Engineer with the Masdar Institute of Science and Technology, Abu Dhabi, UAE. His research interests include applications of power electronics in distribution systems, power quality enhancement, renewable energy, FACTS, and power system optimization.

Mr. Kanjiya was awarded the K.S. Prakasa Rao Memorial Award for earning the highest C.G.P.A at IITD in August, 2011.



Vinod Khadkikar (S'06–M'09) received the B.E. degree from the Government College of Engineering, Dr. Babasaheb Ambedkar Marathwada University, Aurangabad, India, in 2000; the M. Tech. degree from the Indian Institute of Technology (IITD), New Delhi, India, in 2002; and the Ph.D. degree from the École de Technologie Supérieure (ETS), Montréal, QC, Canada, in 2008, all in electrical engineering.

From December 2008 to March 2010, he was a Post-Doctoral Fellow at the University of Western Ontario, London, ON, Canada. From April 2010 to December 2010, he was visiting faculty at the Massachusetts Institute of Technology, Cambridge, MA, USA. Currently, he is an Associate Professor at the Masdar Institute of Science and Technology, Abu Dhabi, UAE. His research interests include applications of power electronics in distribution systems and renewable energy resources, grid interconnection issues, power quality enhancement, active power filters, and electric vehicles.

Dr. Khadkikar is currently an Associate Editor of the *IET Power Electronics Journal*.



Mohamed Shawky El Moursi (M'12) received the B.Sc. and M.Sc. degrees from Mansoura University, Mansoura, Egypt, in 1997 and 2002, respectively, and the Ph.D. degree from the University of New Brunswick (UNB), Fredericton, NB, Canada, in 2005, all in electrical engineering.

He was a Research and Teaching Assistant in the Department of Electrical and Computer Engineering, UNB, from 2002 to 2005. He joined McGill University as a Post-Doctoral Fellow with the Power Electronics Group. He joined Vestas Wind Systems, Arhus, Denmark, in the Technology R&D Group with the Wind Power Plant Group. He was with TRANSCO, UAE, as a Senior Study and Planning Engineer, and seconded as a Faculty Member in the Faculty of Engineering, Mansoura University. He was a Visiting Professor at the Massachusetts Institute of Technology, Cambridge, MA, USA. He is currently an Associate Professor in the Electrical Engineering and Computer Science Department, Masdar Institute of Science and Technology. His research interests include power system, power electronics, FACTS technologies, system control, wind turbine modeling, wind energy integration, and interconnections.

He is serving as an Associate Editor for *IET Renewable Power Generation* and *IET Power Electronics Journals*.



James L. Kirtley Jr. (F'91) received the Ph.D. degree from the Massachusetts Institute of Technology (MIT), Cambridge, MA, USA, in 1971.

He has been with the Large Steam Turbine Generator Department General Electric, and with Satcon Technology Corporation. Currently, he is a Professor of Electrical Engineering at MIT.

Dr. Kirtley served as an Editor-in-Chief of the IEEE TRANSACTIONS ON ENERGY CONVERSION from 1998 to 2006, and continues to serve as Editor and as a Member of the Editorial Board of *Electric Power Components and Systems*. He was awarded the IEEE Third Millennium Medal in 2000 and the Nikola Tesla Prize in 2002. He is a Registered Professional Engineer in Massachusetts and is a member of the United States National Academy of Engineering.

QUERIES

Q1. Author: Please spell out of OPAL-RT, PID, FACTS and C.G.P.A.	760
Q2. Author: Please check whether the edit in the sentence starting: “The dc motor drive power . . .” is ok.	761
Q3. Author: Please provide page range in Ref. [6].	762
Q4. Author: Please provide location details.	763
Q5. Author: Please check if the edits to the BIOS of author “Vinod Khadkikar” are ok.	764
Q6. Author: Please provide location details.	765
Q7. Author: Please provide field of study.	766
Q8. Author: Please provide location details.	767
	768

IEEE
Proof